THE ULTRAVIOLET CORONAGRAPH SPECTROMETER FOR THE SOLAR AND HELIOSPHERIC OBSERVATORY

J.L. KOHL, R.ESSER, L.D. GARDNER, S. HABBAL, P.S. DAIGNEAU, E.F. DENNIS, G.U. NYSTROM, A. PANASYUK, J.C. RAYMOND, P.L. SMITH, L. STRACHAN and A.A. VAN BALLEGOOIJEN
Harvard-Smithsonian Center for Astrophysics, Cambridge, Massachusetts 02138 U.S.A.

G. NOCI, S. FINESCHI, M. ROMOLI, A. CIARAVELLA* and A. MODIGLIANI
Università di Firenze, I-50125 Firenze, Italy

M.C.E. HUBER
Space Science Dept., ESA/ESTEC, NL-2200 AG, Noordwijk, The Netherlands

E. ANTONUCCI, C. BENNA and S. GIORDANO
Università di Torino, I-10125 Torino, Italy

G. TONDELLO, P. NICOLOSI, G. NALETTO and C. PERNECHELE
Università di Padova, I-35131 Padova, Italy

D. SPADARO
Osservatorio Astrofisico di Catania, I-95125 Catania, Italy

G. POLETTO
Osservatorio Astrofisico di Arcetri, I-50125 Firenze, Italy

S. LIVI
Max Planck Institut für Aeronomie, D-37189 Katlenburg-Lindau, Germany

O. VON DER LÜHE
European Southern Observatory, D-85748 Garching, Germany

J. GEISS
International Space Science Institute, CH-3012 Bern, Switzerland

J.G. TIMOTHY
University of New Brunswick, New Brunswick, Canada E3B 5A3

G. GLOECKLER
University of Maryland, College Park, Maryland 20742 U.S.A.

A. ALLEGRA
Alenia Spazio, I-10146 Torino, Italy

G. BASILE
Officine Galileo, Divisione Ottica e Spazio, I-50013 Firenze, Italy

R. BRUSA
Brusag, CH-8712 Stäfa, Switzerland

B. WOOD
Oerlikon-Contraves, Space Division, CH-8052 Zürich, Switzerland

O.H.W. SIEGMUND
Space Sciences Laboratory, University of California, Berkeley, CA 94720 U.S.A.

W. FOWLER
Ball Corporation, Electro-Optics and Cryogenics Div., Boulder, Colorado 80306 U.S.A.

Solar Physics **162**: 313–356, 1995.

and

R. FISHER and M. JHABVALA
NASA/Goddard Space Flight Center, Greenbelt, MD 20771 U.S.A.

Abstract. The SOHO Ultraviolet Coronagraph Spectrometer (UVCS/SOHO) is composed of three reflecting telescopes with external and internal occultation and a spectrometer assembly consisting of two toric grating spectrometers and a visible light polarimeter. The purpose of the UVCS instrument is to provide a body of data that can be used to address a broad range of scientific questions regarding the nature of the solar corona and the generation of the solar wind. The primary scientific goals are the following: to locate and characterize the coronal source regions of the solar wind, to identify and understand the dominant physical processes that accelerate the solar wind, to understand how the coronal plasma is heated in solar wind acceleration regions, and to increase the knowledge of coronal phenomena that control the physical properties of the solar wind as determined by *in situ* measurements. To progress toward these goals, the UVCS will perform ultraviolet spectroscopy and visible polarimetry to be combined with plasma diagnostic analysis techniques to provide detailed empirical descriptions of the extended solar corona from the coronal base to a heliocentric height of 12 solar radii.

Key words: Sun – Solar Corona – Solar Wind – UV Spectroscopy – UV Coronagraph

1. Primary Scientific Objectives

The Ultraviolet Coronagraph Spectrometer (UVCS) for the Solar and Heliospheric Observatory (SOHO) mission is designed for ultraviolet spectroscopy and visible light polarimetry of the extended solar corona. The primary scientific objective of the UVCS investigation is to identify and understand the dominant physical processes controlling the extended solar corona and the generation of the solar wind, and to understand the relationship of such processes to solar wind properties near the Earth. To progress toward this goal, UVCS is designed to obtain a detailed description of the physical conditions in the extended corona. Ultraviolet spectroscopic techniques are designed to determine the random velocity distributions, the densities and the outflow velocities of the primary particles (i.e., electrons and protons) and of several minor ions. Chemical abundances as a function of height in the extended corona can be derived. This information can be obtained for the large-scale structures such as coronal holes, helmet streamers and active regions, and for substructures of those features such as polar plumes, and the closed magnetic arch structures and open current sheets of helmet streamers. UVCS can also make detailed spectroscopic measurements of coronal mass ejections, and the shock compression and heating of the ambient coronal plasma through which they propagate. Heliographic heights from the coronal base to as high as 12 $R_\odot$ can be observed by UVCS. The long duration of SOHO and its continuous viewing of the Sun allows UVCS to determine the time evolution of the observed coronal structures.

* Also Osservatorio Astronomico di Palermo and Consiglio Nazionale delle Ricerche

The primary scientific objectives of the UVCS instrument are:

To investigate mechanisms for accelerating the solar wind,

To identify the dominant acceleration mechanisms, for example, to determine the roles of thermal pressure gradients (Parker type wind), wave-particle interactions, and suprathermal electrons in accelerating the solar wind in different regions,

To test proposed mechanisms for accelerating heavy ions and producing variations in the chemical composition of the solar wind.

To investigate mechanisms for heating the coronal plasma,

To determine if dissipation of energy carried by MHD waves is a dominant source of plasma heating, particularly in magnetically open regions where heating by MHD waves is a strong candidate for coronal heating,

To distinguish mechanisms for heating ions from those heating electrons, particularly in regions where the coronal plasma becomes collisionless,

To determine the radial variation of the heating in a variety of structures in order to empirically constrain heating mechanisms (*e.g.* power dissipated as a function of height, characteristic dissipation lengths, dependence of these on physical conditions in, and structure of, a variety of regions with magnetically open and closed configurations),

To locate and characterize coronal sources of the solar wind,

To use tomographic techniques on UVCS spectroscopic limb data to provide global maps of the temperature, density, flow velocity and particle flux (as a function of height) from the low corona, where most of the surface appears to be covered with closed magnetic structures, out to several solar radii above the surface where the magnetically open regions expand to occupy the entire volume and the outflow becomes predominantly radial. These global maps can be used to determine which coronal regions are associated with different types of flows measured far from the Sun by *in situ* techniques or radio scintillation techniques,

To provide other possible signatures for distinguishing between sources of low and high speed wind: temperatures, densities, and flow velocities of several types of ions and MHD wave amplitudes,

To determine the role of internal structures in coronal holes in generating high speed solar wind. Polar plumes are raylike structures in polar coronal holes which contain a significant fraction of the mass in these regions and hence could be a source of the solar wind outflow from polar regions. The UVCS has the spatial resolution and spectroscopic diagnostic capability for testing this hypothesis.

To investigate coronal phenomena that establish the plasma properties of the solar wind,

To study the physics of the high temperature coronal plasma as it makes a transition from collision-dominated to collisionless conditions. The solar corona is a useful laboratory for studying this fundamental phenomenon. For many processes the corona, which is collision-dominated near the coronal base, becomes collisionless several tenths to several solar radii above the surface,

To acquire critical data on the ionization balance (temperatures, densities, flow velocities of the electron/proton plasma and heavy ions, and heavy ion abundances) in the region where the solar wind ionization states are *frozen in*, 1.5 $R_\odot \leq r \leq 5\ R_\odot$. These data, in combination with those acquired by *in situ* instruments on SOHO, will provide unique, fundamental data for investigating processes controlling the distribution of heavy ion charge states in the solar wind,

To determine chemical abundances (O, Si, Mg and Fe) and determine their variations in the inner solar wind. Determination of the spatial and temporal variations of the chemical composition at the coronal source of the solar wind is vital to understanding the mechanisms producing the large variations in abundances measured *in situ* far from the Sun.

2. Primary Spectroscopic Diagnostic Techniques

This section briefly summarizes how EUV spectroscopic measurements and visible polarized radiance observations can be used to determine the basic plasma parameters of the solar wind source region. The diagnostic methods, which are used, are well documented (Kohl and Withbroe, 1982; Withbroe *et al.*, 1982a, 1985; Noci, Kohl and Withbroe, 1987 and van de Hulst, 1950) and will therefore not be discussed in detail here. The feasibility and utility of the spectroscopic diagnostics for proton random velocity, and outflow velocity in both coronal holes and quiet coronal regions have been demonstrated with rocket and Spartan 201 observations of HI Ly-α and O VI 1032 Å, 1037 Å (Kohl *et al.*, 1980, 1984; Withbroe *et al.*, 1982b, 1985, 1986; Strachan, 1987; Kohl *et al.*, 1995; Kohl *et al.*, 1994; Strachan *et al.*, 1994). Examples of electron density determinations from white light coronagraphs are described in the literature as well (e.g., Munro and Jackson, 1977).

Proton and ion velocity distributions can be determined from measurements of the spectral line profiles of HI Ly-α, Fe XII 1242 Å, O VI 1032 Å, Mg X 610 Å and Si XII 499 Å. The shape of a spectral line depends on the velocity distribution of the particles emitting or scattering the measured photons. The velocities are produced by thermal motions, nonthermal motions (due, for example, to waves), and bulk outflow velocities in the line of sight. The coronal HI Ly-α profile is strongly affected by thermal motions (130 km s^{-1} at 10^6 K), while the more massive particles tend to be affected most strongly by non-thermal motions. Expected line widths are provided

in Figure 1 along with measurements of the width of HI Ly-α made with a rocket UV coronagraph in a polar coronal hole observed in 1980 (Withbroe *et al.*, 1985).

The velocity distribution of neutral hydrogen in the corona reflects the proton distribution, because the characteristic lifetime for a hydrogen atom at typical coronal densities is significantly shorter than typical coronal expansion times (Withbroe *et al.*, 1982a). For example, at r = 2.5 $R_\odot$ in a low density coronal hole, a newly created HI atom will move about 0.02 $R_\odot$ before it is ionized.

The directly measurable quantity is the velocity distribution along the line of sight. The use of resonance line profiles provides a direct method for measuring coronal velocity distributions. Because the corona is optically thin for the selected lines, the profiles are, effectively, direct measurements of velocity distributions along the line of sight. UVCS provides synoptic observations that can be used to help determine three dimensional models of stable structures such as coronal holes.

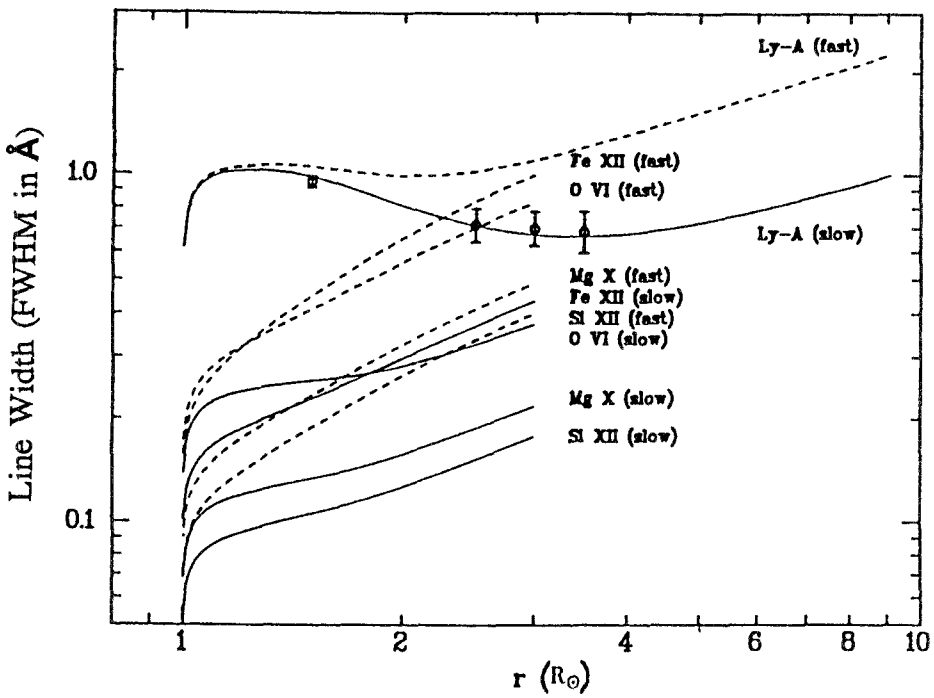

Fig. 1. Estimated line widths of primary spectral lines of UVCS for fast and slow wind.

Electron temperatures and velocity distributions are determined from the coronal line profile of the electron scattered component of HI Ly-α. The electron component of coronal HI Ly-α is produced by Thomson scattering of chromospheric HI Ly-α by electrons in the extended corona. This means

of measuring coronal electron temperatures was first suggested by Hughes (1965). The electron component has the approximate form:

$$I_e(\lambda) = const \int_{-\infty}^{\infty} N_e exp(-(\lambda - \lambda_0)^2/\Delta\lambda_e^2) dx \quad (1)$$

where $\Delta\lambda_e$ is the Doppler width and x is along the line of sight. Because of the high thermal velocity of electrons at coronal temperatures (nearly 7000 km s^{-1} for $T_e = 1.5 \times 10^6$ K) the effects of solar wind flows and nonthermal motions on the shape of the profile can be neglected. This profile is much wider ($\sim$ 50 Å) than the resonantly scattered component ($\sim$ 1 Å). An empirical model must be used to take into account small effects on the profile shape due to the Thomson scattering process (see Withbroe *et al.*, 1982a).

Electron densities can be determined by measuring the polarized radiance of the visible corona with the visible light section of the UVCS. The percent polarization of the observed intensity can be determined by measuring the polarized radiance at 0°, +60° and -60° (cf. Billings, 1966). This eliminates the F corona which is expected to be unpolarized at heights up to 5 $R_\odot$ and also eliminates unpolarized stray light. The Thomson scattering process that gives rise to the K-corona is well understood and the techniques enabling the electron density to be determined from the polarized radiance have been employed with eclipse and satellite data for a number of years. These techniques require that the coronal polarized radiance be determined relative to the spectral irradiance of the solar disk.

Electron densities can also be measured using the intensity of the electron-scattered component of HI Ly-α. Since the Ly-α emission from the F corona is much narrower than the broad electron-scattered component of Ly-α, the Ly-α emission from the F corona can be subtracted without having to use a polarizer.

Outflow velocity determinations in the extended corona will be based on observations, off the limb, of Doppler dimming (Hyder and Lites, 1970) and on spectral line shifts due to the mean value of the outflow component in the direction of the observer. Examples of Doppler dimming calculated for an isothermal corona with a temperature of 1.5×10^6 K are shown in Figure 2.

There are several ways of determining Doppler dimming. One method originally used by G. Noci to analyze Ly-α data from the 1970 eclipse, makes use of the intensity ratio between the resonant component of a line such as HI Ly-α, O VI 1032 Å, or Mg X 610 Å and electron scattered visible light. The ratio

$$\frac{I_r}{I_{WL}} = const \times A_{el} < R_i >< D_i(V_W) > \quad (2)$$

where A_{el} is the elemental abundance, $< R_i >$ is the ionization balance term and $< D_i(V_W) >$ is the Doppler dimming term plotted in Figure 2.

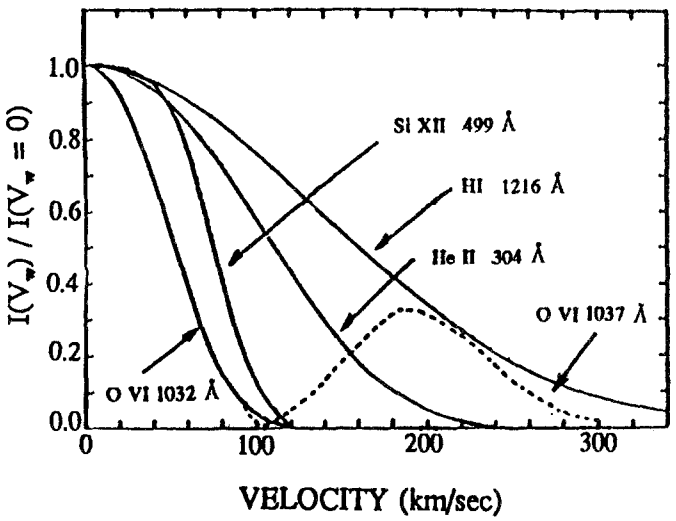

Fig. 2. Doppler dimming of resonantly scattered coronal radiations

Measurements of the intensity ratio as a function of radius can be used to determine the amount of Doppler dimming and, hence, the bulk outflow velocity of the observed ions. Spectral lines of different ions can have different sensitivities to outflow velocity.

A definitive analysis requires an empirical model which uses as inputs, measured electron temperatures and electron densities. This information is used in the model to calculate the ionization balance terms R_i and predict the observed EUV intensity as a function of the outflow velocity. Since the outward particle flux must be conserved, the models can provide self consistent predictions of the Doppler dimmed EUV lines as a function of height.

It is highly desirable to use several complementary methods to determine outflow velocities. For example, the required electron densities can be determined from both visible light and Thomson scattered Ly-α (the latter eliminates the radiometric calibration uncertainty from Doppler dimming analyses of Ly-α). An indication of supersonic outflow in a coronal structure from Doppler dimming would usually imply that the observed spectral line should be shifted by a measured amount (this provides a self consistent check).

The dimming of the O VI line at 1037.613 Å is particularly useful because pumping by C II 1037.018 Å extends its velocity sensitive range to include values from 90 km s^{-1} to 250 km s^{-1} (Noci, Kohl and Withbroe, 1987). Pumping by C II occurs when the O VI outflow velocity is large enough that the C II profile of the incoming light from the lower atmosphere is

red shifted onto the coronal O VI scattering profile in the rest frame of the outflowing O VI. The dashed line in Figure 2 shows the effect.

Because Doppler dimming only affects the resonantly scattered component of spectral lines and lines of O VI and Mg X have collisional components, it is necessary to determine the relative intensity contributions of the two mechanisms. Kohl and Withbroe (1982) and Noci, Kohl and Withbroe (1987) have shown that the intensity ratio of the resonance line doublet for a lithium-like ion such as O VI or Mg X, determines the relative intensities of the collisionally excited and resonantly scattered components. The collisional component can also be predicted with the empirical model.

In view of the above discussion and determinations of supersonic outflow in a coronal hole within 3 $R_\odot$ of Sun-center (Kohl *et al.*, 1984; Strachan, 1987), it is apparent that Doppler dimming and Doppler shifts can provide a sensitive determination of the magnitude and location of solar wind acceleration in the solar wind source region of the corona.

The intensities of the EUV lines, in combination with the electron temperatures and densities determined from UVCS measurements, can be used to derive abundances of the parent elements (O, Mg, Si, Fe). For ions with resonant doublets measured by UVCS (e.g., O VI, Mg X, Si XII) the value of the collisional component of the line intensity can be determined with the technique described by Kohl and Withbroe (1982) and Noci, Kohl and Withbroe (1987). The result can be used to determine the O, Mg, and Si abundances independently of the outflow velocities. This approach is useful in regions where the collisional component is a significant fraction of the total intensity. The UVCS measurements of electron temperatures, densities and outflow velocities can provide the necessary data for constructing a reliable model on which to base the abundance determinations.

3. Instrument Overview

The SOHO Ultraviolet Coronagraph Spectrometer consists of a telescope spectrometer unit (TSU) and a remote electronics unit (REU) (see Figure 3). The TSU is a triple telescope with external and internal occultation and a high resolution spectrometer assembly. The TSU has its own pointing mechanism, a roll mechanism, a telescope mirror mechanism, an internal occulter mechanism and an aperture door mechanism. Electronics located in the TSU include image processors, detector power supplies and monitors, sun sensor electronics and position transducer electronics. Three spherical telescope mirrors focus co-registered images of the extended corona onto the three entrance slits of the spectrometer assembly. The spectrometer assembly consists of three channels:

- The Ly-α channel is a toric grating spectrometer with an entrance slit mechanism, a neutral density filter inserter, a grating mechanism, and a

windowed crossed delay line (XDL) detector (the Ly-α detector). This channel is optimized for line profile measurements of H I 1216 Å and may also be used for other spectral lines in the 1145 Å to 1287 Å spectral range. An extended wavelength range (1100 Å to 1361 Å) may be observed by rotating the grating.

- The O VI channel is a toric grating spectrometer with an entrance slit mechanism, a neutral density filter inserter, a grating mechanism, and an open XDL detector (the O VI detector). The O VI detector is optimized for measurements of the O VI lines at 1032 Å and 1037Å and may also be used for other spectral lines in the 984 Å to 1080 Å (first order) and 492 Å to 540 Å (second order) spectral range. An extended wavelength range in first and second order (937 Å to 1126 Å and 469 Å to 563 Å, respectively) may be observed by rotating the grating. The O VI channel includes a convex mirror between the grating and the O VI detector to focus the HI 1216 Å (first order) and Mg X 610 Å and 625 Å (second order) radiations onto the O VI detector. That arrangement is called the redundant Ly-α path.
- The white light channel (WLC) is a visible light polarimeter and consists of an entrance aperture, a polarimeter assembly, and a photomultiplier tube. The polarimeter assembly includes a rotatable half-wave plate, a fixed linear polarizer, a bandpass filter and a lens. The WLC measures polarized radiance in the 4500 Å - 6000 Å wavelength band.

The REU electronics include the central processing unit, low voltage power supplies, power switching, mechanism controller circuitry, housekeeping, thermal control and interface electronics.

Typical instrument parameters used for UVCS observations are summarized in Table I. The primary observational mode provides simultaneous and cospatial measurements of the line profile of HI 1216 Å, the integrated spectral radiance of OVI 1032 Å and 1037 Å, Mg X 610 Å and 625 Å, Si XII 499 Å and 521 Å, Fe XII 1242 Å, other spectral lines within the UVCS spectral ranges, and the visible polarized radiance. Other modes provide intensities of other lines, electron scattered HI Ly-α, spectral line profiles for minor ions and higher spectral and/or spatial resolution, but require longer exposure times.

The field-of-view (FOV) of UVCS is illustrated in Figure 4. The instantaneous FOV is the portion of the solar image that passes through the entrance slits of the ultraviolet channels. Spatial elements along the instantaneous FOV are resolved by the XDL detectors. The WLC has a 14 arcsecond x 14 arcsecond spatial field at the center of the instantaneous FOV. Internal mirror motions are used to step the instantaneous FOV across the 141 arcminute direction. Offset pointing adjustments with the UVCS pointing mechanism can be used to extend the FOV down to the solar limb and onto

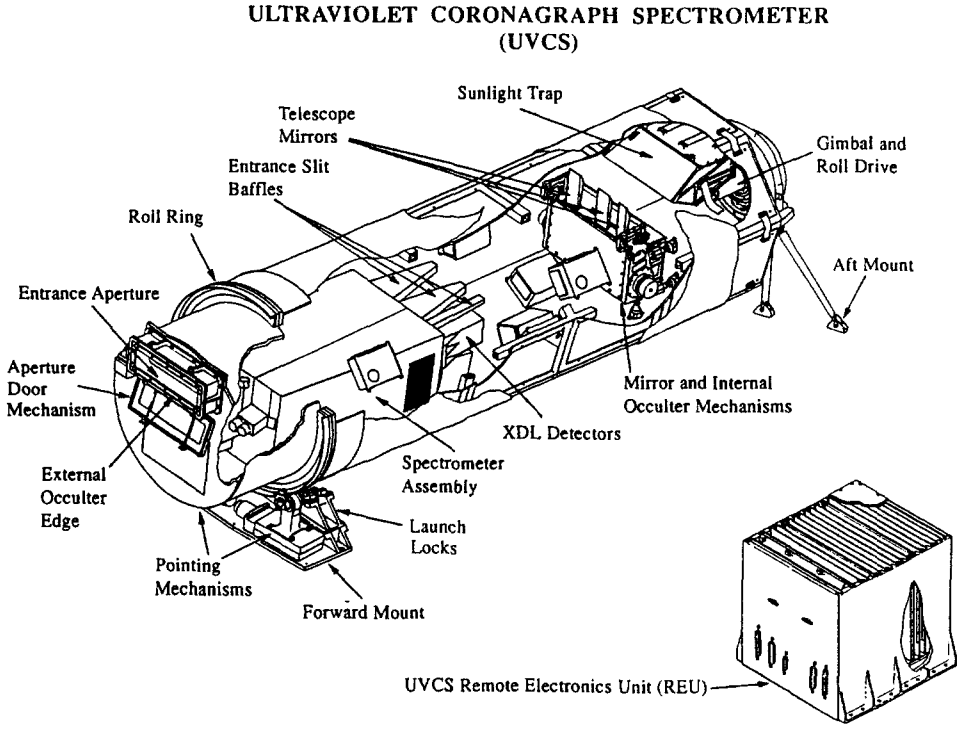

Fig. 3. UVCS Diagram

the disk or up to 12 $R_\odot$. UVCS can rotate its FOV about Sun-center in order to observe the full corona.

4. Occulted Telescope

4.1. Optical Layout

It can be seen in Figure 3 that the UVCS telescope consists of three very similar channels, the principal differences being in the size and surface finishes of the telescope mirrors and in the design of the entrance slit baffles. Figure 5 is an illustration of the optical layout of the H I Ly-α channel which will serve here to represent all three telescope channels. The optical rays are for the case where the center line and roll axis of UVCS are pointed at Sun-center.

TABLE I
Typical Observational Specifications for UVCS

Spectral Line (A)	Observed Quantity	Spectral Resolution FWHM (Å)	Spatial Resolution (*) FWHM
H I 1216	Profile	0.23	12" x 15" - 24" x 24"
H I 1216	e-Profile	2.0	1.7' x 2'
Fe XII 1242	Intensity	1.21	1' x 1'
Fe XII 1242	Profile	0.23	12" x 5'
O VI 1032/1037	Intensity	0.81	1' x 1'
O VI 1032/1037	Profile	0.15	12" x 5'
Si XII 499/521 (2nd order)	Intensity	0.41	1' x 1'
Si XII 499/521 (2nd order	Profile	0.08	12" x 5'
Mg X 610/625 (2nd order)	Intensity	0.41	1' x 1'
Mg X 610/625 (2nd order)	Profile	0.15	12" x 5'
4500 - 6000	Polarized Radiance	1500	14" x 14"

(*) Limited by diffraction at 1 $R_\odot$<r<1.8 $R_\odot$

The primary optical components of each occulted telescope are the entrance aperture, the telescope mirror, the internal occulter, the entrance slit baffle, the entrance slit, and the sunlight trap. There are also a series of telescope baffles and a Sun sensor consisting of four shadow edge sensors.

The entrance aperture is rectangular and consists of three knife edges and a serrated edge that acts as a linear external occulter which shields the telescope mirror from direct sunlight; the knife edges serve to limit the FOV and the amount of solar disk light entering the instrument. The approximately 32 arcminute divergent beam from the solar disk enters the instrument through the entrance aperture, passes through a series of three baffles and within 1.6 mm of the telescope mirror edge. That light then enters the sunlight trap where it is attenuated.

The telescope mirror has a spherical figure with a focal length of 750 mm (see section 4.2). It is placed such that coronal light passing through the entrance aperture from 1.2 $R_\odot$, just reaches the edge of the mirror and

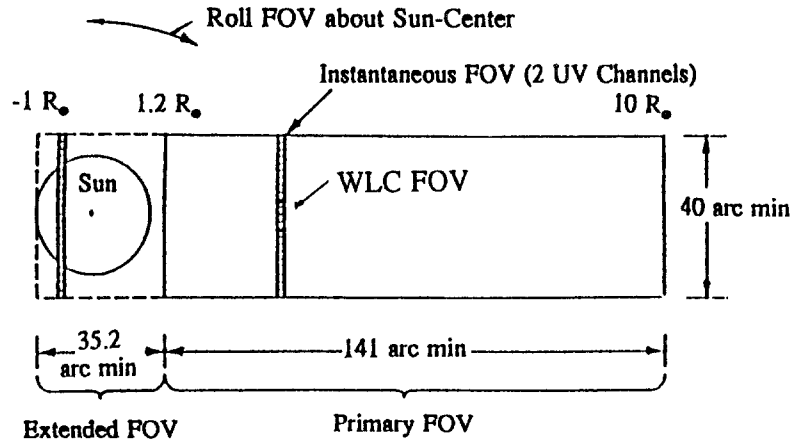

Fig. 4. The field-of-view (FOV) of UVCS

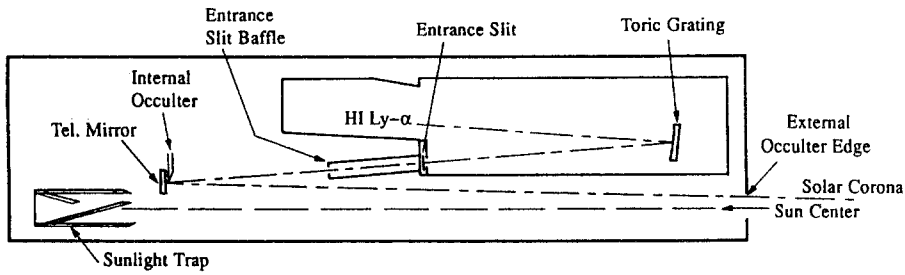

Fig. 5. Optical Layout of the H I Ly-α Channel

coronal light from 10 $R_\odot$ completely fills it. This mirror focusses the coronal light onto the spectrometer entrance slit, which accepts a segment of the coronal image thus defining the instantaneous FOV (see Figure 4). The mirror is rotated to scan the coronal image across the entrance slit. The telescope mirror also images the external occulter inside the spectrometer. This results in an out-of-focus image of the external occulter on the entrance

slit. Most of the solar disk light diffracted and scattered by the external occulter onto the telescope mirror is blocked by the entrance slit jaws.

The purpose of the internal occulter is to intercept that portion of the diffracted and scattered light from the external occulter that would otherwise be specularly reflected by the telescope mirror through the entrance slit. The internal occulter must over-occult in order to compensate for alignment tolerances. Hence, in blocking the light from the external occulter, the internal occulter also blocks that coronal light from the instantaneous FOV that passes near the external occulter and toward the innermost edge of the unvignetted telescope mirror surface. This over-occulting nominally covers a 1 mm wide strip of the otherwise unvignetted mirror area. The unvignetted area of the telescope mirror is given by the following:

$$A = hD \tan[16/60(r - 1.2)] - b \tag{3}$$

where h is the height of the mirror (i.e., its dimension parallel to the limb tangent), D is the distance between the external occulter and the telescope mirror, r is the heliocentric height corresponding to the center of the instantaneous FOV (in $R_\odot$), and b is the over-occulting width. As the mirror is rotated to view various heights in the corona, the internal occulter must also move so as to remove the light from the external occulter that would otherwise be specularly reflected by the mirror into the spectrometer entrance slit.

The entrance slit baffle limits the FOV of the entrance slit to an area that is slightly larger than the telescope mirror, thereby only passing light from the mirror surface, the internal occulter, narrow strips of the mirror masks near the mirror edges that are adjacent to the internal occulter, and a narrow open strip just off the edge of the mirror that is opposite the internal occulter. The sunlight trap must be positioned so the view of the slit through the narrow open strip is into a dark and un-illuminated region of the sunlight trap.

The sunlight trap consists of three regions: two regions which are illuminated by direct solar disk radiation and a dark region between them. One of the illuminated regions is placed so that the line-of-sight from it to the entrance slit is blocked by the telescope mirror and the line-of-sight to the other illuminated region is blocked by the entrance slit baffle. The design of the sunlight trap is discussed in Section 4.3.

4.2. Telescope Mirrors

The telescope mirrors for UVCS are of two types. The mirrors for the uv channels are SiC clad SiC and the visible mirror is Si clad SiC with a Cr overcoating. All three mirrors have spherical figures and radii of curvature of 1502 mm. The mirrors have rectangular cross sections with the uv mirrors

being 72 mm by 50 mm, and the visible mirror being 72 mm by 30 mm (the smaller dimension parallel to the solar limb tangent).

The surface finish is the most critical specification for the UVCS mirrors. Surface roughness values of 8 Å rms were specified for the uv mirrors and 5 Å with a goal of 3 Å for the visible mirror. Those values were most readily achieved on spherical surfaces. The spherical aberration added 7 μm to the total image spread and about $\lambda/4$ wavefront error compared to an off-axis parabola. The distribution of scattered energy is important because the light diffracted from the external occulter edge can be scattered (at small angles from the specular direction) by the telescope mirrors into the entrance slits. Hence, the autocovariance of surface roughness for large autocovariance lengths should be very small and the autocovariance curve should approximate a Gaussian. The quality of the edges around the front surface is also important because aperture masks are not used to cover the edges. A small polished radius ($R < 0.1$ mm) blending into the clear aperture is used to specularly reflect light away from the image.

It is recognized that the chosen surfaces do not provide optimal reflectance at all wavelengths of interest. The SiC clad mirrors provide about 45% reflectance at 1216 Å compared to a typical value of 78% for Al + MgF_2. The Cr coating provides about 65% reflectance for visible wavelengths. Nonetheless, the selected surfaces for the Ly-α and visible channel mirrors were accepted because of problems in manufacturing and time constraints.

4.3. Sunlight Trap and Sun Sensor

The purpose of the sunlight trap is to intercept direct solar radiation which enters the entrance aperture, attenuate it, and conduct and radiate the resulting heat to thermal radiators. A diagram of the sunlight trap is provided in Figure 6. It consists of three cavities, two of which intercept the direct sunlight, and a dark cavity between the others that is within the line-of-sight of the spectrometer entrance slits. The dark cavity is shielded from the direct solar rays by the central baffle (an extension of one of the trap walls) which has a knife edge at its sunward end.

The cavities, which intercept the direct sunlight, are made of polished nickel plated beryllium with a specular black multilayer coating provided by the Optical Filter Corporation. Each cavity has two plates that intercept the solar radiation. They are inclined at an angle of 20°.

The basic concept is to provide specular reflections with minimal scatter per bounce, a reflectivity of less than ten (three) percent per bounce in the uv (visible), and a minimum of seven bounces before specularly reflected sunlight leaves the trap. The surface finish is specified at 20 Å rms roughness to achieve an acceptable level of non-specular reflection.

Specular and non-specular reflectance measurements of sample plates were performed at visible and uv wavelengths to ensure acceptable per-

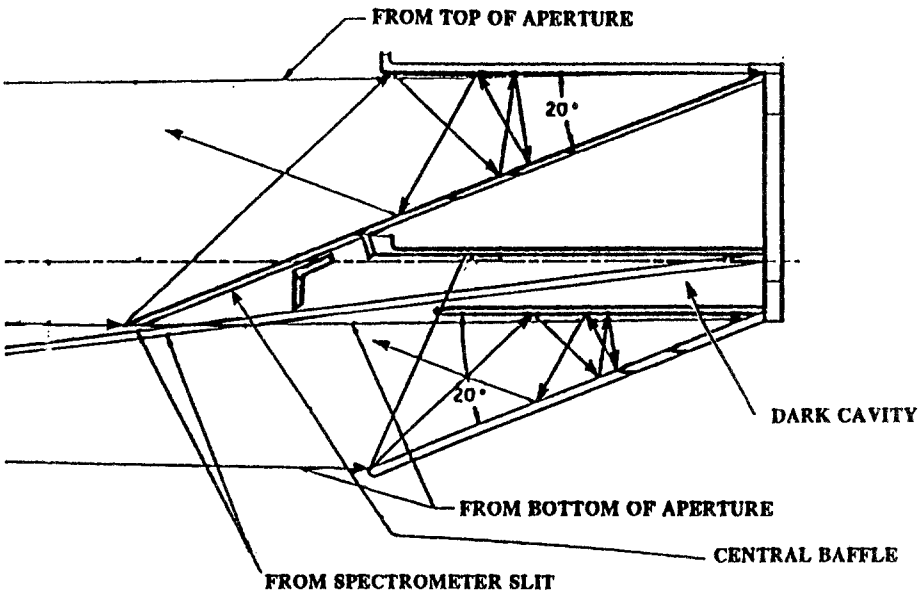

Fig. 6. Illustration of Sunlight Trap

formance. Specular reflectances at angles of incidence between 10 and 70° were measured at 1216 Å, 1840 Å, 2537 Å, and visible wavelengths. The results are more than sufficient to meet the required reduction in irradiance between the trap and the spectrometer entrance slit baffles of about $2x10^{-5}$ for uv wavelengths and about $5x10^{-7}$ for visible wavelengths.

In order to reduce the radiance of the dark cavity to acceptable levels, a secondary baffle prevents sunlight diffracted at the knife edge of the central baffle from entering the cavity, and the interior is coated with a non-specular black material.

The sunlight trap includes four photodiode subassemblies that, together with the entrance aperture, act as a fine Sun sensor (see Figure 7). The photodiodes are positioned to detect light at the edges of the direct sunlight beam. The light level on the diodes depends on the locations of the shadow lines from the edges of the entrance aperture. This information can be used to determine the orientation of the occulted telescope system relative to the Sun for a range of about ±15 arc minutes. The instrument controller determines the orientation from the ratio of the difference to the sum of the light signals from photodiodes on opposite sides of the direct sunlight beam. Holes in the illuminated sunlight trap cavities allow the sunlight to pass through the trap and onto the photodiodes. A bandpass filter is located in front of each photodiode and a baffle tube defines its FOV. The filter and

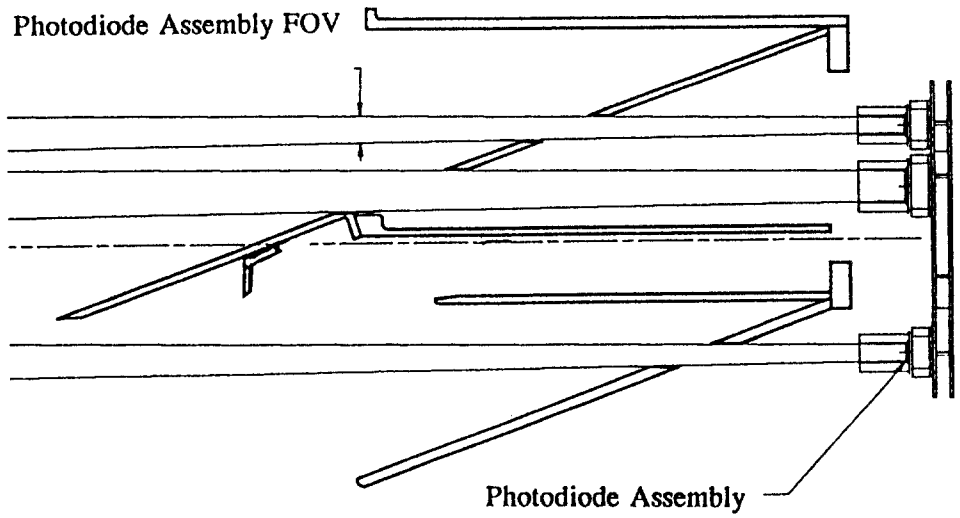

Fig. 7. Photodiode subassemblies and holes provided in sunlight trap to allow sunlight to reach the photodiodes.

diodes are tilted so that the specularly reflected light will not pass back through the holes in the cavities.

4.4. Mirror/Occulter Mechanism

The mirror/occulter mechanism (MOM) consists of independent mirror and internal occulter mechanisms that are jointly controlled and coordinated by the instrument flight software. The three mirrors image segments of the corona on their respective spectrometer entrance slit. The mirror mechanism consists of a mirror/carrier subassembly which supports two ultraviolet mirrors and one coated visible light mirror. These mirrors are aligned and mounted (via lapping and shimming) onto the carrier such that their foci are coaligned to within thirty arcseconds. The mirror/carrier subassembly is supported by flex pivots, actuated by a voice coil actuator (VCA) and has its position sensed by differential impedance transducers (DIT). The VCA and DIT subsystems provide mirror position control, readout precision and repeatability to within 2.5 arcseconds and maintain physically-redundant actuating and sensing elements.

The internal occulter mechanism blocks the portion of each telescope mirror that would otherwise specularly reflect diffracted light from the external occulter into the respective spectrometer entrance slit. The mechanism consists of an occulter plate subassembly supported on each side by thin steel bands which are integrated within a rotational drive system. This drive sys-

tem consists of a drive pulley controlled by a limited-angle torquer motor and sensed by a resolver and an idler pulley subassembly that converts a ±57° drive pulley rotation into the ±36 mm occulter translational range required to occult each mirror for observations from 1.2 to 10 $R_\odot$. The torquer motor/resolver subsystems are physically-redundant and provide internal occulter edge positional control to less than 0.1 mm. The optical characteristics of the internal occulter are discussed in Section 6.

The MOM also maintains independent launch lock mechanisms which utilize paraffin actuators to constrain the mirror/carrier and occulter plate subassemblies during launch and prevent unacceptable mechanical loads from being transmitted through nonstructural elements of the subassemblies. The mirror/carrier and occulter plate launch locks are positioned to place the mirror/occulter at its approximate 2.7 $R_\odot$ position. These actuators then provide the ability to release these launch constraints via instrument command to allow on-orbit mechanism function. The MOM is aligned and integrated within the telescope assembly using a kinematic mount support system of three titanium uniaxis mounts and one three-axis mount assembly. This mount system allows global motions of the MOM during its alignment to the telescope and also isolates differential structural deformations between the interfacing telescope assembly and MOM housing structures.

4.5. Roll/Pointing Mechanisms

The roll and pointing mechanisms allow UVCS to scan heliocentric heights from 1.2 to 12 $R_\odot$ and roll the UVCS FOV about Sun-center in order to observe any position angle, and to correct for any SOHO Sun-center misalignment. The roll mechanism, located at the aft end of the instrument, can rotate the telescope assembly over a ±179.75° range. Rotation is induced by a stepper motor driving a gearhead/harmonic drive which provides an approximate 5000:1 gearing ratio from the stepper motor. Electrical connections between the REU and interior telescope hardware are routed through a flexible lead assembly which maintains a wire-for-wire conductance over the full rotational range. The baseline rotation rate is 8° per minute and variable rates between 3 and 15° per minute are available for implementation through the flight software. The telescope rotational position is sensed by a resolver which allows rotational position control to ± 0.1°.

The offset pointing mechanism allows an offset pitch and yaw pointing of the telescope assembly over a ±54 arcminute range. The telescope roll ring subassembly possesses an integral roll/pointing ring which rests upon two crowned and hardened front support rollers at symmetric positions about the telescope centerline. The rollers are supported by roller bearings mounted by metallic stands which are driven inward and outward by translation stages, providing a bidirectional motion of the telescope assembly. Retention springs integral within the roller bearing subassemblies restrain the telescope

roll/pointing ring onto and maintain constant contact between the ring and the drive rollers. Offset pointing positions within ±16 arcminutes of Sun-center are measured by the Sun sensor (see Section 4.3) while pointing positions outside of this central zone are computed based on position telemetry of the two translation stages. The fine-pointing Sun sensor, which consists of four redundant photodiodes located at positions about the Sun-center reference line, provides a Sun-center determination to within ±4 arcseconds by measuring relative photodiode signal intensities. This fine pointing control can be utilized following roll maneuvers to eliminate any Sun-center misalignment caused by the telescope roll mechanism. The translation stage drive capacity allows offset pointing at a baseline rate of approximately one arcminute per minute, but slower and faster pointing rates are available for implementation through the flight software.

4.6. Aperture Door Mechanism

The aperture door mechanism protects the interior telescope hardware and critical optical surfaces from particulate and molecular contamination during ground operations and on-orbit SOHO attitude control maneuvers. This subassembly, mounted on the forward face of the TSU end cap assembly, consists primarily of the entrance aperture, housing, door and drive sub-assemblies. The forward surface of the housing mounts the entrance aperture, a gold-plated frame with an integral serrated external occulter edge. The occulter edge and plate possess match-drilled interfaces to allow a proper alignment of the instrument occulting system. The remaining aperture edges are also mounted and aligned onto an aperture plate. The door consists of a beryllium structural frame supporting a clear teflon window. Although the primary purpose of this window is for contamination protection, this window also allows 90% of the nominal thermal energy (with door open) to pass into the instrument sunlight trap and maintain a proper thermal balance when the door is closed on-orbit. The door is actuated by a stepper motor gearing network such that when it is open, the door hardware lies completely behind the entrance aperture plane to prevent extraneous light scatter into the aperture. When the door is closed, link springs and two door latches are engaged to lock the door into its closed position. Redundant external microswitches provide a dual indication through instrument telemetry of the door actuation from and to either its open or closed positions.

The baseline door open or close operation requires 45 seconds. Both slower and faster rates are also commandable. For example, the fastest door rate (door closing in about 15 seconds) would be implemented upon receipt of the emergency Sun reacquisition flag signal from the SOHO Spacecraft command system.

5. The Spectrometer Assembly

5.1. The Ly-α and OVI Spectrometer Channels

The UVCS spectrometer assembly has been designed to cover a suitable spectral range according to the scientific requirements. For several reasons, e.g., reflectivity of the optical coatings, large differences in the emitted intensity among the elements of the solar corona and others, it has been designed to accomodate two very similar UV channels. One is optimized at 1216 Å for the observations of the HI Ly-α line and a second one at 1035 Å for the OVI lines at 1032 Å and 1037 Å. Their optical design has also been driven by mechanical constraints on the accommodation of the main optical elements: entrance slits, gratings and detectors. Both spectrometer channels use toric gratings and thus assure stigmatic spectral imaging: a single, albeit aspheric optical surface provides diffraction, reflection and focusing, as well as correction for astigmatism. Given the relatively low reflection coefficients in the vacuum ultraviolet wavelength domain, a single optical surface is optimum with respect to efficiency. Each UVCS grating is used in a Rowland-circle mounting, with a diffraction angle, β, near the grating normal. The horizontal (i.e., spectral) focus of a spherical concave grating lies on the Rowland circle, and the vertical (i.e. spatial) focus lies outside this circle. The Rowland circle has a diameter equal to the horizontal radius of curvature, R_h, of the grating surface. When an originally spherical grating surface is transformed into a toric one by making the vertical radius of curvature, R_v, smaller than R_h, then the vertical (i.e. the stigmatic) focal plane begins to approach the Rowland circle. Eventually, the two focal surfaces touch at $\beta = o^\circ$ and then intersect each other at $\beta = \pm\beta_o$. Both, astigmatism correction and spectral focus occur at the so-called stigmatic points, i.e. where the stigmatic focusing-surface intersects (or touches) the Rowland circle (see Figure 8). The relation between vertical and horizontal radii of curvature of the grating surface, the angle of incidence, α, and the angles of diffraction, $\pm\beta_o$, where the astigmatism is corrected, is (see Figure 9)

$$R_v \,/\, R_h = cos\ \alpha \ \cdot\ cos\,|\,\beta_o|. \tag{4}$$

In the vicinity of the astigmatic foci, i.e., near the angles of diffraction, $\pm\beta_o$, the separation of the spectral and spatial foci along a bundle of light rays is small. Here, the blur remains near the detector resolution and effective stigmatic imaging occurs. As long as β_o is kept small, effective stigmatic imaging can be maintained on both sides of the grating normal over a section of the Rowland circle that slightly exceeds $\approx 2R\beta_o$. In order to reduce the aberrations, it was necessary to keep the angle of incidence α on the gratings small and the diffraction angle β as near as possible to zero. The parameters of the optical design are summarized in Table II.

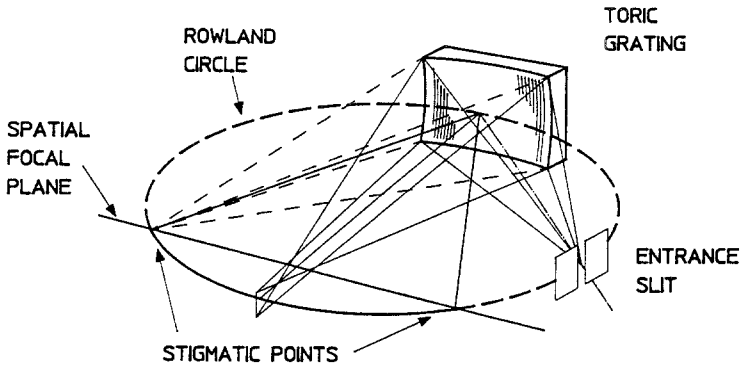

Fig. 8. Isometric display of the imaging properties between the two stigmatic points $\pm\beta_o$.

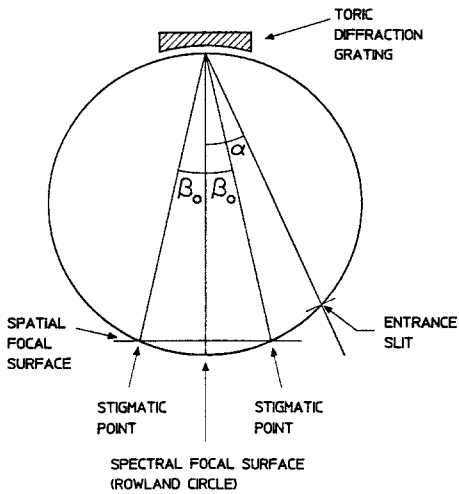

Fig. 9. Schematic of the spectral and spatial imaging of a single toric grating. Exact stigmatic focusing is obtained at angles of diffraction $\pm\beta_o$, which are defined by Equation 5. Given a sufficiently small value of β_o, effective stigmatic focusing (with respect to the pixel size) can be achieved between and somewhat beyond the two stigmatic points.

In order to scan a suitable spectral range through the FOV of the detector, both the gratings can rotate, being mounted in a Johnson (1952)-Onaka (1958) configuration. The best center of rotation of the grating is located at 127 mm from its vertex along a direction nearly perpendicular to the bisector line of the angle between the incident and the diffracted rays. In this way, the grating translates when rotating, always keeping the best spectral focus on the detector. In the OVI channel, a grazing incidence mirror has been mounted (not shown in Figure 9) in order to deviate and focus the Ly-α line radiation on the detector. In this way redundancy is provided for the Ly-α observations.

TABLE II

Optical parameters of the UVCS spectrometer channels.

Ly-α channel	
Ruling frequency	2400 l/mm
Angle of incidence α	12.85°
Angle of diffraction β	3.98°
Main radius of curvature R_h	750 mm
Minor radius of curvature R_v	729.5 mm
Reciprocal dispersion	5.54 Å/mm (1st order)
Spectral bandwidth of pixel	0.14 Å (1st order)
Spatial width of pixel	7" (0.025 mm)
OVI channel	
Ruling frequency	3600 l/mm
Angle of incidence α	18.85°
Angle of diffraction β	2.78°
Main radius of curvature R_h	750 mm
Minor radius of curvature R_v	708.9 mm
Reciprocal dispersion	3.70 Å/mm (1st order)
Spectral bandwidth of pixel	0.0925 Å (1st order)
Spatial width of pixel	7" (0.025 mm)

A preliminary evaluation of the optical performances of the spectrometer has been done through extensive ray-tracings for both the Ly-α and the OVI channels. In Figure 10 some ray-tracing results for the Ly-α channel are reported as examples. The spectral and spatial blurs vs. wavelength for various positions of a point source with respect to the dispersion plane are shown.

From the analysis of these ray-tracings, the following conclusions can be derived regarding the predicted optical performance:

- For point sources near the middle ($\sim$1mm) of the entrance slit, the expected spectral aberrations are considerably smaller than the pixel size (25 μm);
- The same is true for the spatial aberrations near the stigmatic points, i.e. Ly-α and OVI lines; obviously, they increase for wavelengths far from the stigmatic points;
- For points far from the middle of the entrance slit, both the spectral and spatial aberrations increase because of defocusing; the former is greater than 2 pixels for the extreme points;

– All the aberrations are proportional to the illuminated portion of the grating.

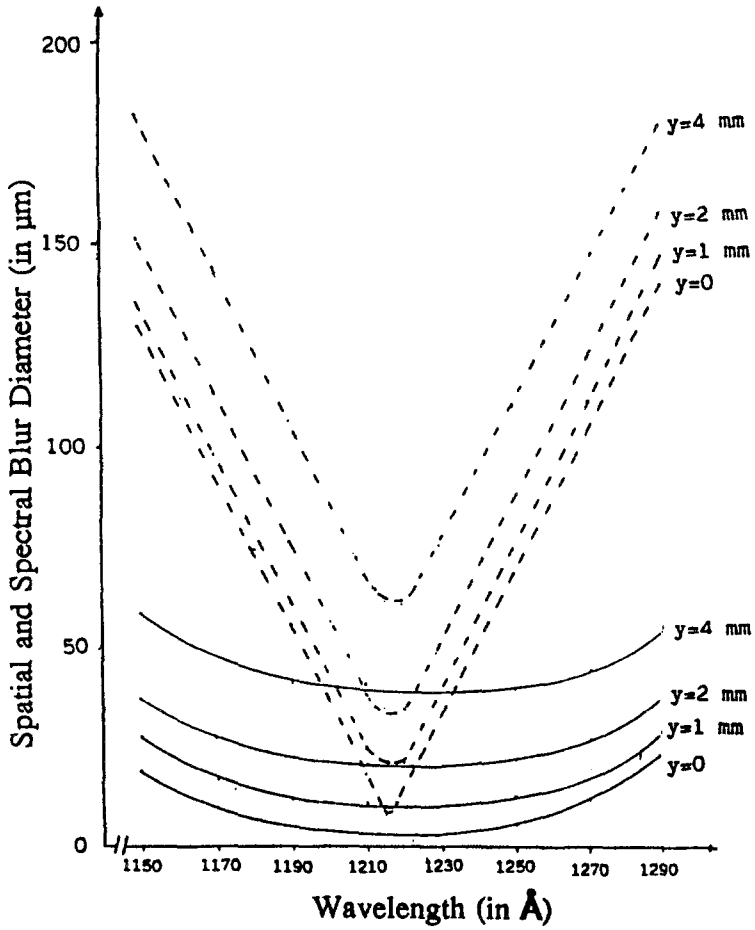

Fig. 10. Predicted spectral (solid) and spatial (dashed) blurs of the Ly-α channel. Several curves for point sources at indicated distances (y) from 0 to 4mm from the middle of the entrance slit are provided.

5.2. Diffraction Gratings

The UVCS gratings are the dispersive optical elements in the two channels of the instrument that give access to the Ly-α line at 1216 Å and to the O VI line at 1032 Å and 1037 Å. Accordingly, the two gratings are designated 'Ly-α' and 'O VI'. They were fabricated, respectively, by holography and on a mechanical ruling engine. The original grating rulings could be produced on spherical surfaces, since the toric surfaces were generated as part of the grating replication process. At one stage of this process, the originally spherical grating was replicated onto an elastic substrate, subsequently "bent"

into a toric grating through controlled deformation, and then replicated in this state.

The performance of toric gratings, produced in this fashion, at extreme ultraviolet (EUV) wavelengths had been verified in the laboratory, by use of MAMA detectors, by Huber *et al.* (1988), following the original work by Haber (1950), Lemaître (1978) and Timothy *et al.* (1989).

Each grating is mounted in a cell under spring-loading so that displacements under vibration and within the acceptable temperature range during flight remain well below one arc-sec. To facilitate the adjustment of the spectrometer before it is put into a vacuum chamber, both the Ly-α and O-VI gratings are equipped with two sets of alignment rulings which are placed on both sides of the main ruling.

The alignment rulings make the visible (5460.7 Å) and ultraviolet (2537 Å) Hg-I spectral lines appear at the location of the prime solar ultraviolet lines. In this way, the alignment of the grating can be tested under atmospheric conditions both visually and by use of a uv-sensitive detector. Special diaphragms, that are part of the grating cells, cover the alignment rulings in the flight configuration, so that the main ruling only is exposed to solar radiation.

The Ly-α and the O-VI gratings are coated with Al+MgF_2 and Ir, respectively. The O VI grating is also used in 2nd order so that the radiation from minor ions—in addition to O VI — like Mg X and Si XII become accessible to measurement.

Furthermore, the straylight properties of the holographic Ly-α grating are such that a direct measurement of the coronal electron temperature appears feasible. This measurement is taken from the shape of the very wide, weak line-wings of the fluorescent coronal Ly-α line, that are caused by Thomson scattering of the Ly-α radiation emerging from the chromosphere.

Measurements during laboratory tests indicate overall efficiencies of 23% and 10% for the Ly-α and O-VI gratings, respectively; Fineschi *et al.* (1994).

5.3. Entrance slit mechanisms

The image of the solar corona is projected by the telescope mirrors onto the entrance slits of the spectrometer. Their width can be varied in order to optimize the spectral resolution and count rate requirements for a particular observation. Identical entrance slit mechanisms for each UV spectrometer channel accomplish slit width variation.

Each slit is formed by two components: a lower edge that is fixed and directly mounted on the interface flange, and a movable upper edge that is connnected to the moving part of a parallelogram.

The slit width is measured by linear variable differential transducers measuring the stroke of the movable edge. This edge is translated by a high-precision parallelogram linkage motor which is connected to a bearing-pinion

engaged with a cam driven by a stepping motor. The primary widths are 355, 213, 53, 25 and 10 μm and the slit height is 8.73 mm. The specified repeatability and readout of the width is $\pm 1 \mu$m.

For each slit, the slit-edge, which corresponds to the smaller solar radius, is placed at a common location. Accordingly, the near disk image edge of the slits for all spectrometer channels are co-linear within 0.3 μm in the dispersion direction and within 2 μm along the mirror focal direction. In order to prevent possible internal stray light from entering the spectrometer, the entrance slits are shielded by entrance slit baffles. The two baffles, one for each UV spectrometer channel, are cylinder-shaped with internal rectangular diaphragms for stopping inner reflections.

5.4. Filter inserter mechanism

For calibration purposes, it is foreseen to observe the solar disk. In this case the positioning of a filter in the optical path is required. For this operation a mechanism has been designed for each channel and has been attached to the interface flange of the entrance slits. The movement is accomplished with a limited angle torque motor and readout with a rotary variable differential transducer.

The main requirements of the filters are the following. They will cover the full optical aperture in each channel and will provide a 1×10^{-3} attenuation at 1216 Å for the UV channels and 1×10^{-3} attenuation at 4500-6000 Å for the WLC. They will be placed in the optical path on command and will be fail-safe in the "out" position. To satisfy the fail-safe requirements, an antagonist spring has been introduced with the rest position keeping the filter completely out of the light path of the slit.

5.5. Grating mechanism

Grating mechanisms position the diffracted spectrum on different parts of the detectors, keep the gratings stable in a certain position during the data acquisition and scan the spectral lines across the detector pixels. According to the already mentioned grating optical properties, in order to hold spectral focus the grating has to be both rotated and translated. For this reason the axis of rotation is not through the optical vertex of the grating. In Table III are the functional requirements specified for the mechanism.

The grating mechanism is illustrated in Figure 11. The grating is mounted in its housing which is directly connected to the rotation axis by two arms that accommodate flexural pivots. Flexural pivots have been introduced because the needed rotation is too little to be performed by a bearing system and furthermore the absence of rotating components reduces lubrication and contamination problems.

A voice coil actuator is inserted in the mechanism for the grating positioning. In this kind of motor there is no contact between the rotor and the stator

TABLE III

Functional requirements of the grating mechanism.

Range for Ly-α channel	$\pm 0.5°$ Position 1216 Å (± 4 Å) on any pixel (dispersion direction only).
Rotation axis for Ly-α channel	127 mm from center ray intercept with optic.
Range for OVI channel	$\pm 0.5°$ Position 1032 Å (± 4 Å) on any pixel (dispersion direction only).
Rotation axis for OVI channel	127 mm from center ray intercept with optic.
Placement Precision	0.014 Å
Readout accuracy	0.007 Å
Stability during an observation	± 0.005 Å
Step Size	0.005 Å

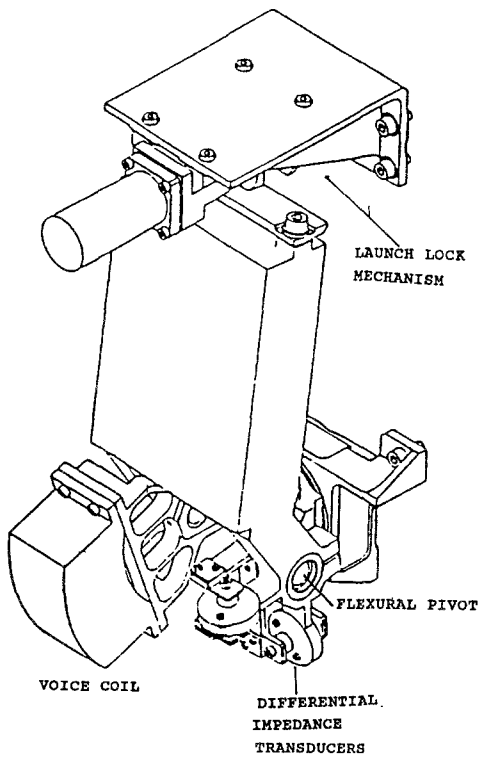

Fig. 11. Grating drive mechanism.

and, according to its characteristics it is possible to use it for both coarse and fine movement. The control action is performed by two pairs of differential impedance transducers: this measuring system provides exceptional resolution, repeatability and nulling accuracy for detecting the aligned and centered position of the conductive target relative to a pair of non-contacting

sensors. This is the way in which the system works: for differential measurement applications, two precisely matched sensors are positioned on opposite sides or ends of a target; as the target moves away from one sensor it moves toward the other an equal amount so that a differential, bipolar output is available.

These mechanisms include launch locks. These locks introduce a constraint in the z direction perpendicular to the grating surface and a limited clearance in the other two directions in such a way as to limit the grating housing motion. The blocking action is obtained by two shaped wheels mounted on a stepper motor axis. The rotation of 180° of this axis changes the position of these wheels and presents sectors where the wheels work as stops. In this way, the gratings are locked for shipment and launch with the primary spectral lines positioned on the center of the detector arrays.

5.6. Delay Line Detectors for UVCS

The detectors developed for UVCS are two dimensional photon counting, centroiding, microchannel plate sensors with electronic readout. Two virtually identical detectors are used for the Ly-α and O VI channels of the spectrometer assembly. A KBr coated, low resistance Z stack of microchannel plates (MCP's) provides detection and amplification, and a multilayer cross delay line anode (XDL) accomplishes position readout. The format is 26 $mm \times 9$ mm, electronically digitized to 1024×360 pixels. This detector and its detailed performance characteristics are discussed by Siegmund *et al*, (1994). KBr photocathode material is deposited directly on the MCP Z stack as an opaque layer. Incoming photons interact with the photocathode, resulting in photoelectron emission (Siegmund *et al*, 1987; Siegmund *et al*, 1990) and a subsequent charge avalanche in the MCP's, giving an overall charge multiplication of $\sim 2 \times 10^7$. This charge cloud is drifted from the MCP output to the delay line anode. Here the charge is divided equally between two orthogonal sets of charge collection fingers on the XDL in the X and Y axes. These are connected to X and Y external serpentine delay lines (Siegmund *et al*, 1994) so that the X and Y photon event centroid positions may be deduced from the signal arrival time differences at the two ends of each delay line. The KBr photocathode quantum detection efficiencies (QDE), which were measured prior to installation in the instrument, for both UVCS detectors is given in Table IV. The photocathodes are solar blind, cutting off at about 1600 Å.

MCP photon event pulse amplitude distributions are narrow (<30% FWHM for O VI) allowing amplitude discrimination of background events if desired. The overall background rate is low, with a rate of <1 event cm^{-2} s^{-1} uniformly distributed across the FOV. This was expected for intrinsic beta decay MCP noise (Siegmund *et al.*, 1988; Fraser *et al.*, 1987) for 40KΩ in the Philips MCP glass. Single pixel spot image event counting rates in excess of

TABLE IV
Quantum Efficiencies of UVCS Detectors

Wavelength	Ly-α	O VI
490	0.329118	0.312955
537	0.275157	0.271169
584	0.209053	0.269847
616	0.229963	0.254656
671	0.160996	0.205307
718	0.118657	0.138327
736	0.106493	0.104327
834	0.193081	0.182457
877	0.194705	0.231734
920	0.212977	0.237192
988	0.271909	0.22376
1026	0.19204	0.201065
1066	0.201424	0.228862
1152	0.230254	0.25555
1216	0.17005	0.176085
1335	0.110827	0.106753
1463	0.0420851	0.0360635
1560	0.00514912	0.00374012
2537	6.25538e-06	2.55582e-06

100 events/pixel/sec have been achieved with no degradation of the MCP gain. The detector is stable to better than 1 pixel for global counting rates up to $> 5 \times 10^5$ events s^{-1}, with a calibrated photometric rate/deadtime characteristic (<40% dead time @ $> 5 \times 10^5$ events s^{-1}). The thermal drift is <1 pixel over the expected UVCS temperature range. Flat field images are dominated by MCP fixed pattern noise and are stable, however the expected MCP multifiber modulation is at an unusually low level (a few %). The Ly-α detector has an optically flat MgF_2 entrance window, thus blocking out all thermal ions or electrons from the detector, and all wavelengths <1100 Å. The O VI detector is "open face" with a 90% transmission mesh, biased at +15V, for attenuation of low energy ions, placed 9mm in front of the MCP's at the entrance to the detector vacuum housing. A feature of the XDL system is a commandable artificial pulse (stimulation pulse) injected into each delay line at a rate of $\sim$ 40 sec^{-1}, resulting in a spot image effectively at the center of the detector aperture. The data obtained from this feature gives an in orbit evaluation of electronics health. A number of other command and diagnostic functions are provided for the XDL detectors. Specific

types of command functions include high voltage control, signal threshold level adjustments, and stimulation pulser control. Housekeeping data also includes power supply voltage monitors, X and Y pulse height data, fast event counters, and temperatures.

5.7. Image Processors

The XDL detectors are 2-dimensional photon counting devices; there are 1024 pixels in the spectral (X) direction and 360 pixels in the spatial (Y) direction. The Ly-α and O VI subsystems each have an associated image processor (IP). The IPs process detector data in real time.

Each IP has two image table random access memories (RAMs), one for the X direction on the XDL array and one for the Y direction. Together these image table RAMs contain the "detector mask" which defines the active area on the detector and specifies how events from different pixels on the detector are to be binned. Each IP also contains one image RAM, or accumulator array, which contains the event count for each bin, *i.e.*, the number of times an event is detected in a certain pixel or group of pixels.

An image is accumulated as follows. Each time a photon is detected, the X and Y coordinates of the pixel in which the event occurred are passed to the corresponding IP. The IP electronics either rejects the event or converts the (X,Y) coordinates into an address A in the accumulator arrays. The conversion is done as follows. Coordinate X (a number between 1 and 1024) is fed into the address side of the X image table RAM, and the contents AX at this address is read out. Similarly, the Y coordinate (a number between 1 and 360) is fed into the Y image table RAM, producing a number AY. If AX and AY are both nonzero, AX and AY are concatenated into a single address A, and the contents of this address in the accumulator array is incremented by one, causing the event to be counted. On the other hand, if either AX or AY is zero, the event is rejected (not counted). These functions are performed electronically (i.e., not by software) at a rate of up to 10^6 times per second.

A detector mask consists of the 1024 AX values and 360 AY values contained in the image table RAMs. The active area on the detector consists of those rows and columns with nonzero values of both AX and AY. Events in pixels with the same (AX,AY) combination will be counted in the same "bin" of the accumulator array. Hence, neighboring rows and/or columns on the detector can be combined into an array of super-pixels.

Before an image can be accumulated, a detector mask must be loaded into image table RAM from the REU. Detector masks must be generated on the ground and uplinked prior to reading into the IP. The REU can store up to six detector masks per XDL detector. Each mask will consist of up to five rectangular areas (panels) placed at arbitrary locations on the XDL array, and with uniform size of the super-pixels.

TABLE V
Characteristics of the White Light Channel Polarimeter

Entrance Pinhole	
Size	$50\,\mu m \times 50\,\mu m$
Transmission:	$1x10^{-3}$
$\lambda/2$ Achromatic Retarder	
Clear Aperture:	35 mm
Retardance:	0.5 ± 0.01 waves at 4500-6000 Å
Transmission:	> 90%
Fast Axis Direction:	7.5° (rel. to the polarizer axis)
Polarizer	
Clear Aperture:	35 mm
Type:	Polaroid HN38S
Axis Direction:	0° (rel. to the UV slit length)
Principal Axis Transmission:	60%
Lens	
Focal Length:	124.8 mm
Diameter:	40 mm
Magnification:	-0.5
Transmission:	> 90%
Bandpass Filter	
Type:	Bandpass (4500-6000 Å)
Transmission:	> 50% (average)
Detector	
Type:	EMI 9130B photomultiplier
Active Area:	5 mm diameter circle
Photocathode:	S-20
Window:	borosilicate glass
Quantum efficiency:	> 15% at 4500 – 6000 Å
Dark Countrate:	180 counts/sec

Instrument configuration data and exposure timing data are added to the science data prior to telemetry.

The photomultiplier tube forms the core of the visible light detection system. Data from the visible light subsystem is accumulated into two visible data buffers, which are also operated in ping-pong mode. Since the amount of visible light data is rather small, a number of visible light measurements are collected in one of the buffers before the data are transmitted.

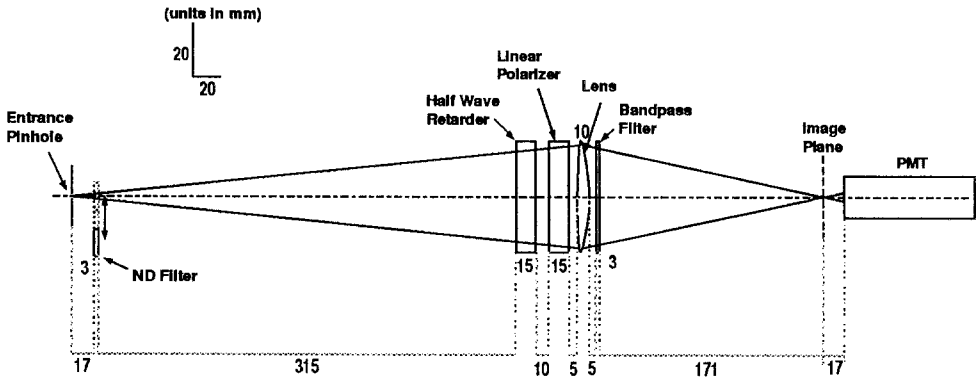

Fig. 12. Optical layout of the White Light Polarimeter

5.8. The White Light Channel

The White Light Channel polarimeter is housed inside the spectrometer assembly. The polarimeter is designed to measure the broadband (4500–6000 Å) linearly polarized radiance of the solar corona between 1.5 and 5 $R_\odot$, and consists of three main subassemblies: the entrance pinhole, the polarimeter group, and the detector. The three channels are aligned along the optical axis which is defined by the entrance pinhole and the center of the telescope mirror. Figure 12 shows the optical layout of the white light polarimeter.

The image of the solar corona is formed by the telescope mirror on the plane of the entrance pinhole, a square $50\,\mu m \times 50\ \mu m$, which selects a spatial element of 14 x 14 arcseconds. Behind the entrance pinhole, a neutral density filter can be inserted to be used for solar disk observations. The radiation from the pinhole goes through the polarimeter group, and is collected by the detector. Table V summarizes the characteristics of the polarimeter optical components.

The optical components of the polarimeter are the half wave retarder plate, linear polarizer, lens, and passband filter (4500–6000 Å). The four components share the same optical axis and are fixed with the exception of the half wave retarder plate, which rotates around the optical axis.

The half wave retarder plate is the active component for the measurement of the linearly polarized radiance and consists of a stack of three polimeric birefringent plates following the achromatic configuration of Pancharatnam (1955), whose fast axis forms alternatively $+30°$ or $-30°$ with the final fast axis of the achromatic plate. In order to measure the linearly polarized radiance the retarder plate is rotated into 3 positions with angular separations

of 30°. The central position has been optimized to maximize the S/N ratio of the measured polarized radiance. The linearly polarized radiance, pI, is then given by the formula:

$$pI = \frac{4}{3}\sqrt{I_o^2 + I_+^2 + I_-^2 - I_o I_+ - I_o I_- - I_+ I_-} \tag{5}$$

where I_o, I_+, and I_- are the radiance measurements for each position of the retarder plate.

The linear polarizer is a dichroic Polaroid HN38S with the transmission axis parallel to the UV slit length direction. In this way, the polarizer always selects radiation that has the same plane of polarization, thus reducing the errors due to the possible sensitivity to polarized radiation of the optical components that follow the polarizer in the optical path.

The lens focuses the light from the pinhole on a plane in the proximity of the detector. The passband filter selects the wavelength range 4500–6000 Å to meet the requirements of achromaticity of the retarder plate and the bandpass of both the polarizer and the detector.

The detector for the WLC is a photomultiplier tube, model EMI9130B, with S–20 photocathode, and low dark count rate, designed to work in the photon counting mode (the detector characteristics are listed in Table V.

The photocathode is positioned out of the image plane of the entrance pinhole in order to increase the maximum measurable signal, and to decrease the instabilities due to spatial inhomogeneities of the photocathode efficiency. The beam size is chosen to be not larger than 2 mm in order to meet the alignment requirements.

6. Stray Light Suppression

Stray light suppression is the most demanding technical requirement for a coronagraph, and a successful design allows UVCS to convey on the entrance slits of the spectrometer a stray light level that is less than most of the coronal signals planned to be detected.

In addition to the occulted telescope stray light suppression, there are stringent stray light requirements on the Ly-α channel of the spectrometer. UVCS plans to measure the electron scattered Ly-α profile in order to determine the coronal electron temperature. The electron scattered Ly-α profile is a broad line ($\sim$ 50 Å FWHM) superposed on the much stronger and narrower ($\sim$ 1 Å FWHM) Ly-α resonant line. Therefore a grating with a good stray light rejection is needed, together with a blocker strip mounted on the detector face that prevents the Ly-α resonant line from reaching the detector.

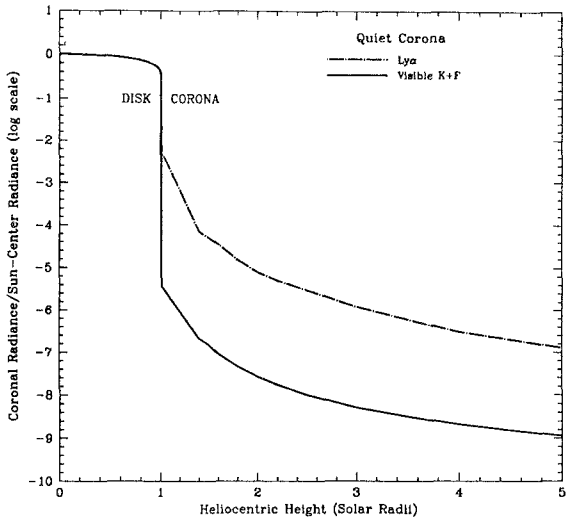

Fig. 13. Ratio of the radiance of a quiet coronal equatorial region to the radiance of Sun-center in HI Ly-α and visible light versus heliocentric height (in $R_\odot$).

6.1. Coronagraph stray light suppression

The approach to stray light suppression in the UVCS is based on the design of a rocket-borne UV coronagraph [Kohl *et al.* (1978), Kohl *et al.* (1980)]. In the following, an analysis of the stray light properties of the UVCS is described [see Romoli *et al* (1993) for a more detailed description of the analysis for the white light channel]. The analysis is based, in part, on measurements of component characteristics. It is shown that internal and external occulters, light traps, baffles, and telescope mirrors are expected to keep the stray light on the entrance slits at an acceptable level.

The problem is well defined in Figure 13, where the radiances of the solar disk and corona in units of the Sun-center radiance are plotted as a function of the heliocentric height. The HI Ly-α radiance in a coronal hole [Strachan (1990)] is plotted, as well as the combined contributions of the visible K and F coronae in a quiet region [Allen (1964)]. The comparison shows that the required stray light suppression in the visible light range is greater than in the UV.

In a coronagraph the solar disk radiation is the source of the stray light. For convenience, the stray light can be divided into two major components: that resulting from radiation that enters the instrument directly, and that which is diffracted by the edges of the entrance aperture. The first contribution can be reduced with a sunlight trap which would ideally absorb or reflect away 100% of this radiation. The second contribution can be reduced by configuring the optical geometry to prevent the light from reaching the

TABLE VI
Sources of stray light in UVCS

- Stray light due to scattering from the light trap
  - o Trap Knife Edge
  - o Trap Surface
- Stray light due to diffraction off the external occulter
  - o Mirror Surface
  - o Mirror Edge
  - o Internal Occulter
- Other stray light contributions
  - o Multiple Non-Specular Reflections off Structural Elements
  - o Aperture Secondary Edges
  - o Off-Band Stray Light
  - o Light Leaks

detection system. In the latter case, this must be done at very little expense of coronal radiation (in the first coronagraph the Lyot stop performed this job). The geometry of the UVCS occulted telescope has been designed in such a way that the level of stray light at the spectrometer entrance slits is lower than most coronal signals planned to be detected. Hence, the telescope environment provides the suppression. It is expected that the primary components of stray light at the entrance slit have very little or no polarization. An effective reduction in stray light is then introduced in the WLC when light is passed through the polarimeter and the polarized light component is determined. In addition, the FOV of the polarimeter has been designed to not intercept some of the potentially significant sources of stray light, such as that from the outer edges of the entrance slit baffle, which is suppressed by a second entrance slit baffle.

Hence, the analysis of the stray light described here has been divided, primarily, into two categories: the stray light involving scattering off the sunlight trap and the stray light due to diffraction off the external occulter. Table VI summarizes the sources of stray light that are classified in the two categories plus four other sources.

Figure 14 summarizes the results obtained. The plot shows the expected stray light irradiance level on the slit in units of solar disk irradiance versus the heliocentric height for each analyzed contribution of stray light and their total, compared with the estimated signal irradiance at the entrance slit. The ordinate gives the irradiance in units of photons cm^{-2}, normalized to the expected solar irradiance at 1 AU. Figure 14a refers to the analysis for HI Ly-α, and Figure 14b refers to the analysis for the visible broadband light.

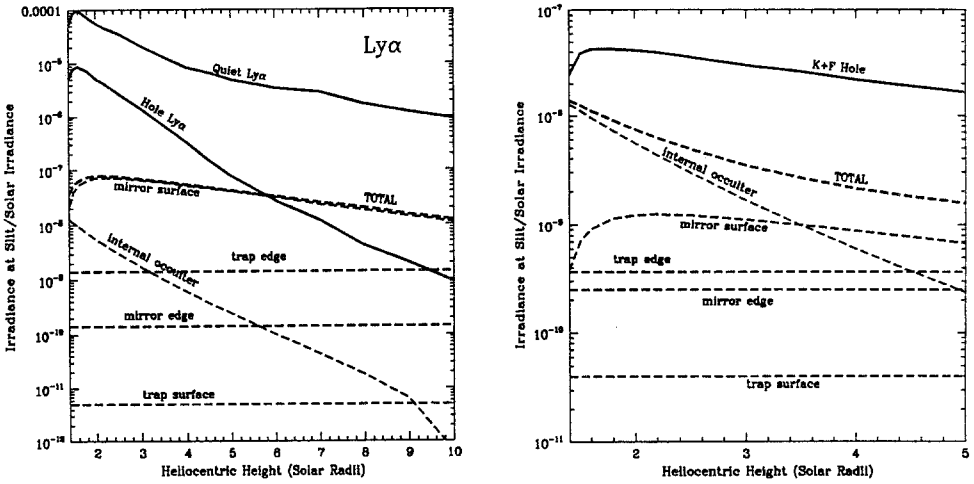

Fig. 14. Signal and stray light irradiances at the slit relative to the solar disk irradiance versus the heliocentric height at Ly-α wavelength (a) and at 4500–6000 Å(b). The solid curve is the signal, the dotted curves are each stray light contribution and the dashed curve is the total stray light contribution.

It is clear from Figure 14a that the major contribution to stray light at Ly-α is expected to come from non-specular reflections off the mirror surface (the primary contribution was originally diffracted by the primary occulter). For visible light, two contributions are dominant. At lower heliocentric heights ($\leq 2.5\,R_\odot$) scatter off the internal occulter is dominant, while above $2.5\,R_\odot$ the contribution from the mirror surface prevails. For the WLC, the effect of the stray light contribution is to increase the statistical error of the polarized radiance derived from the measurement.

6.2. Ly-α Channel off-band stray light suppression

There are two primary off-band scatter requirements for UVCS. Both are for UV wavelengths. The first to be discussed is scatter of near UV and visible radiations by the occulted telescope. Because of the high light levels in the near UV and visible, the combined stray light irradiance for these wavelengths at the entrance slit are much larger than the irradiances for a single UV spectral line. The dispersion of the grating and the spectral variation in the detector sensitivity is needed to further suppress the detected

off-band stray light. In general, one can expect a reduction of better than $1x10^{-6}$ in the near UV and $1x10^{-9}$ in the visible.

The other requirement is needed to suppress resonantly scattered HI Ly-α radiation when observing the broad electron scattered line profile resulting from Thomson scattering of chromospheric HI Ly-α in the corona.

The off-band scatter specifications of the UVCS Ly-α spectrometer channel state that the integrated intensity in the central 5 Å band of the line (i.e., at the diffraction angle) should be 10^4 or greater of the integrated intensity in any 5 Å band between ± 4 to ± 100 Å on either side of the primary diffraction angle.

In order to accomplish this requirement, the Ly-α grating was produced by holography in order to obtain better stray light properties than those for mechanically ruled gratings. In addition, the Ly-α resonant line is blocked by an opaque strip mounted in front of the Ly-α detector face to avoid the saturation of the detector and scatter in the detector window. The blocker is placed in such a way that in the grating launch lock position it does not block any line of interest in the wavelength range of the Ly-α channel, but, when the grating is moved to perform the electron scattered Ly-α profile measurement, the strip completely blocks the Ly-α resonant line for unvignetted telescope areas used for observations up to 4 $R_\odot$.

7. Instrument Characterization and Expected Performance

The UVCS characterization was accomplished in three stages. Throughout the UVCS development, optical components and mechanisms were characterized to ensure compliance with design goals. Optical characterization of the spectrometer assembly was performed at the time of its integration and alignment (Pernechele, C., Naletto, G., Nicolosi, P., Poletto, L., Tondello, G., Proc. SPIE, 2517, 1995). The performance tests of the integrated instrument included calibrations of the mechanisms, radiometric and photometric efficiencies, stray light suppression, spectral and spatial resolutions, spectral and spatial scales, and scattering of a spectral line into its line wing.

Figure 15 shows a schematic layout of the vacuum chamber used for the system level performance tests. The UVCS was supported on an optical bench that could be articulated to acheive alignment with the chamber optics. The chamber provided a solar divergent beam that was large enough to fill the UVCS aperture. This was accomplished by placing a circular field stop (4.2 cm in diameter) at the focal surface of the collimating mirror, and illuminating them with appropriate light sources. A light trap, similar to the one used in the UVCS instrument, simulated a very low radiance corona for the stray light tests. For calibrations in dispersed light, a monochromator could be placed with its exit slit at the collimator focus. Calibrated photo-

diodes mounted on translation stages were used to scan the incident beam and determine incident irradiance levels.

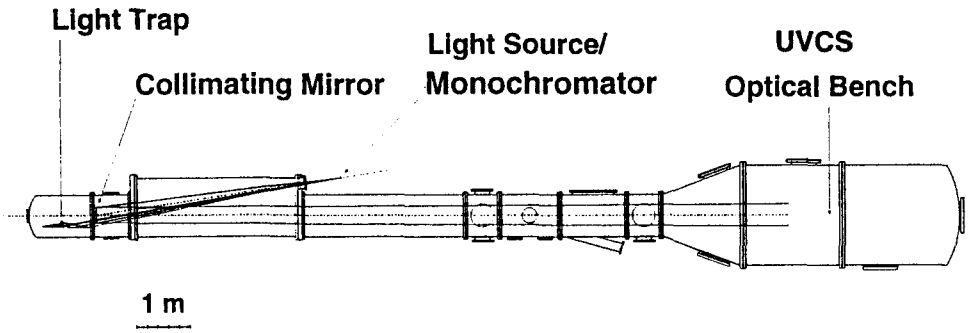

Fig. 15. Schematic layout of the calibration chamber used for the UVCS characterization.

The results of the UVCS characterization are summarized in Table VII The efficiency values are the ratio of the instrument count rate to the measured incident photon rate. It includes the effects of the optical components and detector, but is independent of the instrument aperture and slit width. Off-band efficiency refers to detection of 2537 Å light when the spectrometer is set for 1216 Å. The stray light levels are provided as the ratio of the measured straylight level (described as an equivalent coronal radiance) to the radiance at disk center. Spectral and spatial resolutions are provided as the FWHM of the instrument response to a narrow spectral or spatial source. Because of technical limitations and time constraints, all calibrations were for the instrument aperture used for observations at a heliocentric height of 2.7 $R_{\odot}$. Because of light source limitations, the spectral resolution for the OVI channel is only an upper limit on the size of the resolution element. The stray light levels are all upper limits since there may be contributions from the test chamber. Also, because of light source limitations, the stray light level for the O VI channel was measured at 1236 Å using the redundant Ly-α path. The value of $< 5 \times 10^{-8}$ was obtained before several refinements to the measurement that resulted in the value of $< 1 \times 10^{-8}$ for the Ly-α channel. It is likely that the O VI channel also has a suppression of $< 1 \times 10^{-8}$. All values provided in Table VII are representative of the instrument during the test, but must be updated throughout the mission.

TABLE VII
Measured UVCS Performance Parameters

Instrument Channel	λ (Å)	Efficiency	Straylight	Spectral Resolution (Å)	Spatial Resolution (arc seconds)
Ly-α	1216	0.002	$< 1 \times 10^{-8}$	0.23	15
Ly-α	2537	$< 3 \times 10^{-9}$*			
Redundant Ly-α	1216	0.001	$< 5 \times 10^{-8}$	0.31	15**
O VI	1032	0.0035	$< 5 \times 10^{-8}$***	<0.24	15**
Visible	5460	0.004	$< 1.5 \times 10^{-8}$	4500-6000	15

* With instrument configured to detect 1216 Å
** Inferred from other measurements
*** Derived from redundant Ly-α channel measurement

8. Electronic Layout

The UVCS instrument maintains electronics subassemblies within the TSU and the REU as shown in Figure 16. The TSU-mounted electronics include subassemblies for the differential impedance transducers (not shown), Sun sensors, image processors, and the XDL detectors. The Sun sensor electronics utilize difference and summing amplifiers to translate relative photodiode signals into a fine-resolution solar-center pointing sensor. The image processor utilizes first-in-first-out buffers, detector column and row mask RAMS and a one-microsecond cycle-time state machine for proper data integration. The XDL detector subsystems include detector head subassemblies with integral high-voltage power supplies and amplifier modules. The amplifiers contain high speed and pulse amplitude amplifiers for the delay line signals and the XDL time-to-digital converter electronics contain constant fraction discriminators, time-to-amplitude converters and analog-to-digital converters to decode the detected signals and define event addresses. The XDL monitor electronics provide command and housekeeping activities to operate and monitor the delay line detector.

The REU subassemblies including the central processing unit (CPU) electronics, low-voltage power supplies (LVPS), power switching electronics, mechanism controller circuitry, housekeeping, thermal control and interface electronics are shown in Figure 16. There are two physically-redundant CPU boards (card CPU A and CPU B) within the REU, each containing

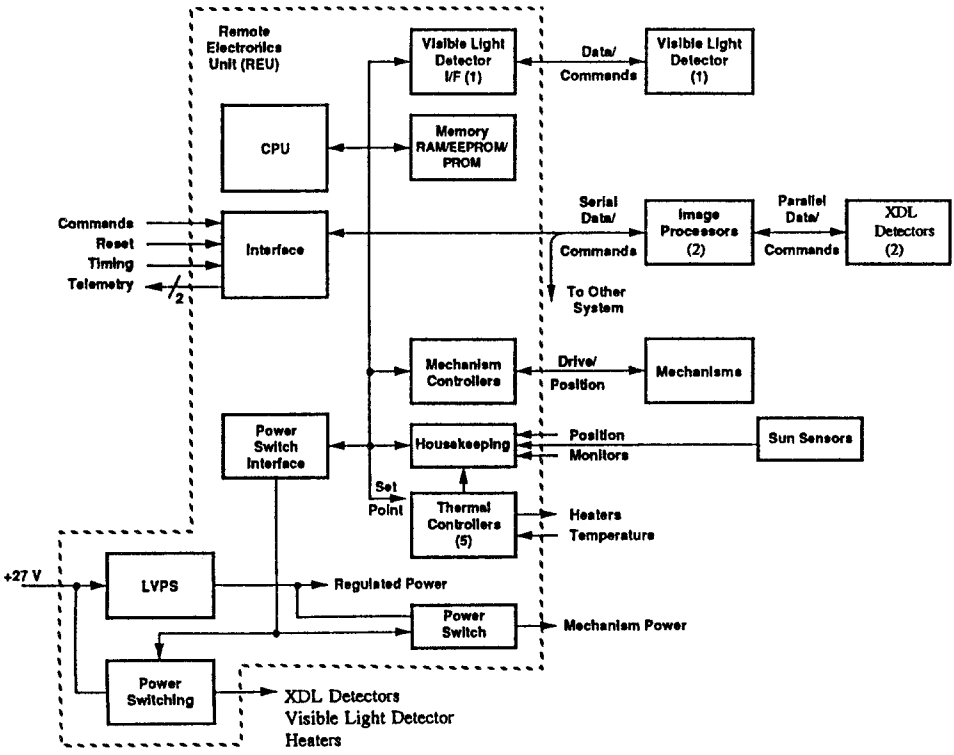

Fig. 16. UVCS Electronic Block Diagram

an experiment controller (EXCON) 80C86-type microprocessor with 5 MHz clock speed and associated 4K by 16-bits of fusible-link read-only memory (PROM), 128K by 16-bits of electrically-erasable programmable memory (EEPROM) and 32K by 16-bits of RAM. The PROM contains "bootstrap" code to allow instrument restart and initialization. The EEPROM is used to upload and modify observing sequences and to modify system configuration parameters during flight. The EEPROM also allows revised flight software uploads. The RAM is primarily used for temporary image storage.

The low-voltage power supplies provide regulated +5V, ±6V and ±15V and switchable ±6V, physically-redundant and independently integrated on two REU printed circuit board (PCB) assemblies. A power-switching pulse code modulation (PCM) assembly provides the necessary level of power establishment and control. Four types (3 closed-loop and one open-loop control) of mechanism controllers are integrated within three PCB assemblies. Critical position controllers for the mirror, occulter and grating mechanisms employ proportional-integral (PI) control architecture. Housekeeping electronics are maintained on one PCB assembly and provide multiplexed, differential-input position and monitor information through a CS5016 analog-to-digital converter for transmission on the 133 bit-per-second SOHO telemetry system. The instrument grounding and power distribution network utilizes a single-point grounding structure with appropriate line isolation. Open-loop thermal control in the form of pulse-width-modulated heater power control exists to maintain appropriate instrument temperature distributions. The single-card interface electronics provide the appropriate command and telemetry decoding and timing electronics to adequately function via SOHO-initiated commanding and telemetry.

The REU employs surface mount technology of passive components for PCB assembly economization.

9. Thermal Design

The UVCS thermal control system employs passive and active means to maintain proper instrument temperature distributions during all phases of the SOHO mission. Passive control hardware such as thermal radiators, multilayer insulation (MLI) and thermal films and finishes are employed on the instrument exterior to maintain proper instrument external thermal exchange with the neighboring SOHO hardware and environment. The aft thermal radiators exchange the high heat dissipations from the sunlight trap and XDL detector electronics with the exterior environment. The telescope assembly MLI maintains interior heat energy and allows a more uniform temperature distribution while its outer indium-tin-oxide coating maintains blanket conductivity and eliminates a source of static charge buildup. Films and finishes such as silverized teflon and gold paint provide low-absorbance, reflective barriers where instrument hardware such as the door interior and roll ring front surface are directly exposed to solar heat energy.

Active control measures include the use of nonoperational and operational heater banks. Nonoperational heaters, which maintain a capacity of 89.7 Watts and are powered (upon SOHO-initiated command) by an independent 27-volt power bus, maintain instrument hardware within nonoperational survivable temperature limits during the pre-operational phases of the SOHO mission. Instrument operational heaters are duty-cycle modulated to

achieve various desired power levels and are used in an open-loop heater control system. These heaters maintain a capacity of 41.2 Watts which is based on minimum instrument operation during beginning-of-life cold-case conditions.

The TSU hardware, with the exception of the front support assembly (FSA), is individually-controlled apart from the SOHO payload module thermal system. The REU and the FSA are collectively-controlled with the interfacing SOHO payload module hardware.

10. Flight Software

The UVCS flight software resides in the REU. The software performs the following functions: (1) instrument control; (2) spacecraft interface; (3) mechanism control; and (4) image processing. The instrument control software includes software for all observing and standby modes. This includes "housekeeping" software to monitor instrument health and to safeguard the instrument against over-exposure of detectors by direct sunlight. The spacecraft interface software is responsible for reception of commands and telemetry of science and housekeeping data. Mechanism control software performs the functions required to safely operate instrument mechanisms. Image processing software performs the functions related to the operations of the image processors (loading of detector masks, taking an exposure).

The flight software provides the user with the capability to operate the instrument interactively (only during contact periods) or in batch mode. Most UVCS observations will be performed by executing "observation sequences" stored in onboard memory. The sequences contain detailed information about UVCS instrument configuration, exposure times, etc. Occasionally new or revised sequences will need to be generated and uplinked in order to address specific scientific objectives or correct for problems with the instrument. The UVCS workstations at the EOF contain the software tools needed to generate, uplink and verify new sequences and associated parameter data.

11. Instrument Commanding And Data Handling

11.1. Commanding

For UVCS we can distinguish three types of command procedures:

- SMOCC Procedures, in which commands originate from a workstation in the SOHO Mission Operations Control Center (SMOCC) and are uplinked to the spacecraft. These procedures will be mainly used during turn-on and checkout of the instrument;
- IWS Procedures in which commands originate from the UVCS Instrument Workstation (IWS) in the Experiment Operations Facility (EOF).

These commands are then routed to the SMOCC (via the EOF Core System) and uplinked to the spacecraft in a near-realtime or delayed commanding mode;
- On-Board Stored Procedures (a.k.a. observation sequences), in which commands originate from the sequence library of the UVCS on-board computer.

SMOCC procedures and IWS procedures must be executed during the near-realtime commanding periods each day. Pointing and roll maneuvers will be performed in the near-realtime commanding mode, at least initially. The most common mode of operation will be to uplink an on-board stored procedure (such as a scan pattern) or a parameter table (such as a detector mask) from the IWS, then issue a command to start the procedure in realtime or at a specified later time.

11.2. Data Handling

Realtime and playback telemetry data will be received at the EOF, while the final flight data will be sent to SAO and the Italian Data Analysis Centers. In either case, the telemetry sorter will separate science data from housekeeping data and convert the UV detector data to image format. At the EOF, quick-look images will be used to verify data quality for planning purposes, to produce the daily summary data files for the ECS, and to carry out some preliminary scientific analyses. The Data Reduction and Analysis Facility (DRAF) at SAO will produce and distribute the definitive data set from the final flight data. Data products to be distributed to investigators and to the SOHO data archive include the following:

1. *Spectral Data Files*: These are FITS files containing uncalibrated detector count data (counts per pixel), as well as instrument configuration and exposure timing data. Each observing sequence will produce one spectral data file per detector.
2. *Visible Light Data Files*: These are FITS files containing the time series of count rates from the WLC, along with pointing information and information on the polarizer and neutral density filter. Each VL data file will contain the data corresponding to one observing sequence.
3. *Calibration Data*:
   a) Parameter files for pointing, spatial, wavelength and radiometric calibrations (ascii)
   b) Flat field and dark count data (FITS)
   c) SOHO orbit and attitude data
4. *Image Data Files, including synoptic maps*: These are FITS files such as the Ly-α maps of the corona to be provided as part of the Summary Data.

5. *Auxiliary Data Files*: These include the disk irradiance history (as determined from periodic pointings at the solar disk), measurements of the instrument profile, stray light data, and pulse height distribution data.
6. *Data Catalogs*: These will include a database to permit users to select observations based on pointing, observation date, type of feature observed, or other criteria. They also include the Mission Log File, which records the observing sequences and other commands sent to the instrument, as well as an evaluation of the data quality.
7. *Data Analysis Software*: This IDL software is used for display and analysis of the science data. It can read and write FITS format Spectral and Visible Light Data Files, display the 2D spectral data, carry out the calibration procedures to correct for instrument response, perform wavelength and pointing calibrations, and transform the science data into physical units (photons cm^{-2} s^{-1} $Å^{-1}$ $ster^{-1}$), and perform some basic functions for measuring line profiles and intensities. Software will also be available to transform a set of spectra covering different radial and roll positions into images, including the daily images to be provided to the Experimenters Control System (ECS) as part of the Summary Data. The Data Analysis Software will be used at various sites including the EOF and Experiment Analysis Facility (EAF) at Goddard Space Flight Center, the DRAF at SAO, the Italian Centers, the Multi-Experiment Data and Operations Center (MEDOC), and other co-investigator institutions. It will require the calibration files listed above as well as the final orbit/attitude files supplied by NASA to determine the pointing from the instrumental parameters and to wavelength and flux calibrate the spectral data files.

Acknowledgements

The UVCS instrument is the result of the work of many individuals and organizations. Although we will not attempt to list every name, we wish to thank and acknowledge the contributions of each person who contributed to the instrument development. They include managers, engineers and scientists at Alenia, Ball Electronics and Cryogenics Division, Composite Optics Inc., ESTEC, Goddard Space Flight Center, Hyperfine Corporation, Observatoire de Marseille, Officine Galileo, Oerlikon-Contraves, Optical Filter Corporation, Smithsonian Astrophysical Observatory, United Technologies Inc., Atomic Ltd., and The University of California at Berkeley. Especially, we wish to thank K. Sizemore, D. Machi, P. Rabino, J. Shannon, B. Sherman, R. Blum, and P. Sozanski for their skillful program management. We also wish to thank W. Koldewyn, R. Novaria, J. Burkepile, R. Reinker, S. Varlese and W. Frank for managing the instrument development at the Ball Electronics and Cryrogenics Division. Special recognition for

extra effort and dedication go to N. Adler, B. Bach, W. Blanco, P. Carosso, R. Carter, J. Coberly, M. Coyle, M. Dami, N. Galluccio, P. Giordano, D. Leviton, J. Marriott, S. Reynolds, M. Tardy, and R. Voorhees. We particularly thank C. Berner, D. Bock, D. Dale, V. Domingo, F. Felici, K. Kirby, A Poland, and I. Shapiro for their extra efforts in accommodating the specific requirements of the UVCS program. The UVCS instrument is the result of the knowledge, skill and efforts of many talented persons including the following who deserve special mention: J. Austin, M. Bartuli, K. Belmont, D. Boyd, S. Burcar, N. Carosso, J. Chappell, E. Ciancetta, A. Cisbani, L. Condello, A. Copty, R. Czichy, R. Faust, G. Ferrari, S. Fike, R. Gemma, J. Girard, D. Hassler, D. Herhager, C. Highman, D. Hill, D. Hillis, M. Honsa, M. Kilpatrick, R. Koehler, D. Langjahr, E. Lear, R. Mathews, A. Melikian, G. Mondello, T. Moran, M. Ostaszewski, P. Pellegrino, L. Poletto, H. Radford, D. Reisenfeld, F. Rivera, D. Rose, L. Suedmeier, M. Vitali, S. Wenners, S. Woolaway, and K. Yoshino. The UVCS program is indebted to the XDL detector team at the University of California at Berkeley and Lockheed including: M. Gummin, T. Sasseen, B. Welsh, G. Gaines, J. Hull, P. Jelinski, R. Raffanti, J. Stock, J. Tom, T. Magoncelli and E. Hertzberg. Thanks also to P. Martens, B. Fleck, and L.D.Sanchez for their extra efforts toward UVCS. We thank C. Hickey of the Harvard College Observatory, and Peter Dandridge Sr. and Peter Dandridge Jr. of Atomic Limited for their work in preparing for the UVCS end-to-end test. We thank W. Parkinson for stimulating discussions and wise council. We also thank the following members of the UVCS Science Team: J. Armstrong, P. Bochsler, A. Bürgi, W.A. Coles, A. Galvin, G.A. Gary, M. Hagyard, L. Hartmann, J. Hollweg, F. Ipavich, E. Jannitti, M. Karovska, G. Lemaitre, R. Kopp, M. Machado, M. Malvezzi, S. Massaglia, M. Messerotti, R. Moore, F. Reale, B. Rickett, R. Rosner, S. Suess, G. Timothy, G. Tozzi, and H. Weiser. We thank those at NASA Headquarters and Agencia Spatiali Italiano for their extra time and talents which were so vitally important to this program. A very special thank you to L. Gagliardi for his dedication to the program and his high standards of excellence. Finally, we wish to thank B. Bernard for her many contributions to the UVCS program including the coordination and preparation of this manuscript. The UVCS program is supported by the National Aeronautics and Space Administration under contract NAS5-31250 to the Smithsonian Astrophysical Observatory, by Agencia Spatiali Italiano and by Swiss Funding Agencies.

References

Allen, C. W.: 1964, *Astrophysical Quantities*, The Athlone Pr., Univ. of London, 175
Billings, D.E.: 1966, *A Guide to the Solar Corona*, Academic Press, New York
Fraser, G.W., Pearson, J.F., and Lees, J.E.: 1987, *Nucl. Instrum. & Meth.* **A254**, 447
Haber, H.: 1950, 'The torus grating', *J. Opt. Soc. Am.* **40**, 153

Huber, M.C.E., Timothy, J.G., Lemaître J.S., Tondello, G., Jannitti, E., and Scarin, P.: 1988, 'Imaging extreme ultraviolet spectrometer employing a single toric diffraction grating: the initial evaluation', *Appl. Opt.* **27**, 3503

Hyder, C.L., and Lites, B.W.: 1970, *Sol. Phys.* **14**, 147

Kohl, J.L., and Withbroe, G.L.: 1982, *Astrophys. J.* **256**, 263

Kohl, J.L., Weiser, H., Withbroe, G.L., Noyes, R.W., Parkinson, W.H., Reeves, E.M., Munro, R.H., and Macqueen, R.M.: 1980, *Astrophys. J.* **241**, L117

Kohl, J.L., Weiser, H., Withbroe, G.L., and Zapata, C.A.: 1984, *Bull. Amer. Astro. Soc.* **16**, 531

Kohl, J.L., Gardner, L.G., Strachan, L., Fisher, R., and Guhathakurta, M.: 1995, *Space Sci. Rev.* **72**, 29

Kohl, J.L., Gardner, L.G., Strachan, L., and Hassler, D.M.: 1994, *Space Sci. Rev.* **70**, 253

Kohl, J. L., Reeves, E. M., and Kirkham, B.: 1978, 'The Lyman Alpha Coronagraph' in van de Hucht, K. A., and Vaiana, G., ed(s)., *New Instrumentation for Space Astronomy*, Pergamon, New York, 1978, 91

Kohl, J. L., Weiser, H., Withbroe, G. L., Noyes, R. W., Parkinson, W. H., Reeves, E. M., Munro, R. H., and MacQueen, R. M.: 1980, *Ap. J.* **241**, L117

Lemaître, G.: 1978, 'Coma and Astigmatism Compensated by Elastic Relaxation on Each Mirror Pair of a Two-Mosaic Telescope' in F. Pacini, W. Richter, and R. N. Wilson, Eds., ed(s)., *Optical Telescopes of the Future*, European Southern Observatory: Garching bei munchen, 321

Munro, R.H., and Jackson, B.V.: 1977, *Astrophys. J.* **213**, 874

Noci, G., Kohl, J.L., and Withbroe, G.L.: 1987, *Astrophys. J.* **315**, 706

Pancharatnam, S.: 1955, *Proc.Indian Acad.Sci* **A41**, 137

Pernechele, C., Naletto, G., Nicolosi, P., Poletto, L., Tondello, G.: 1995, *Proc. SPIE* **2517**,

Romoli, M., Weiser, H., Gardner, L. D., Kohl, J. L.: 1993, *Appl. Opt.* **32**, 3559

Siegmund. O.H.W., M.A. Gummin, J. Stock, D. Marsh, R. Raffanti, T. Sasseen, J. Tom, B. Welsh, G. Gaines, P. Jelinsky, J. Hull, B. Higgins, T. Magoncelli, J. W. Hamilton, S.J. Battel, A. I. Poland, M. Jhabvala, K. Sizemore, and J. Shannon: 1994, *Proc. SPIE* **2280**, 89-100

Siegmund, O.H.W., E. Everman, J. Vallerga, J. Sokolowski, and M. Lampton: 1987, *Applied Optics* **26(17)**, 3607 - 3614

Siegmund, O.H.W. and G. Gaines: 1990, *Proc. SPIE* **1344**, 217-227

Siegmund, O.H.W., Vallerga, J., and Wargelin, B.: 1988, *IEEE Trans. Nucl. Sci.* **NS-35**, 524

Strachan, L., Kohl, J.L., Weiser, H., and Withbroe, G.L.: 1993, *Astrophys. J.* **412**, 410

Strachan, L., Jr.: 1990, *Measurement of Outflow Velocities in the Solar Corona*, Ph.D. Thesis, Harvard University,

Strachan, L., Gardner, L.D., Hassler, D.M., and Kohl, J.L.: 1994, *Space Sci. Rev.* **70**, 263

Timothy, J.G., Morgan, J.S., Slater, D.C., Kasle, D.B., Bybee, R.L., and Culver, H.E.: 1989, 'MAMA detector systems: a status report', *SPIE Ultraviolet Technol. III* **1158**, 104

van de Hulst, H.C.: 1950, *Bull. Astron. Inst. Nether.* **11**, 135

Withbroe, G.L., Kohl, J.L., Weiser, H., Noci, G., and Munro, R.H.: 1982b, *Astrophys. J.* **254**, 361

Withbroe, G.L., Kohl, J.L., Weiser, H., and Munro, R.H.: 1985, *Astrophys. J.* **297**, 324

Withbroe, G.L., Kohl, J.L., and Weiser, H.: 1986, *Astrophys. J.* **307**, 381

Withbroe, G.L., Kohl, J.L., Weiser, H., and Munro, R.H.: 1982a, *Space Sci. Rev.* **33**, 17